**Supplementary Information**

# Rational design of heterogenized molecular phthalocyanine hybrid single-atom electrocatalyst towards two-electron oxygen reduction

Wenjun Fan,[1] Zhiyao Duan,*[2] Wei Liu,[3] Rashid Mehmood,[1,4] Jiating Qu,[1,4] Yucheng Cao,[1,4] Xiangyang Guo,[1] Jun Zhong,[5] and Fuxiang Zhang*[1]

[1] *State Key Laboratory of Catalysis, Dalian National Laboratory for Clean Energy, Dalian Institute of Chemical Physics, Chinese Academy of Sciences, Dalian, 116023, China.*

[2] *State Key Laboratory of Solidification Processing, School of Materials Science and Engineering, Northwestern Polytechnical University, Xi'an 710072, P. R.China.*

[3] *State Key Laboratory of Fine Chemicals, School of Chemical Engineering, Dalian University of Technology, Dalian, 116024 China.*

[4] *University of Chinese Academy of Sciences; Beijing, 100049, China.*

[5] *Institute of Functional Nano and Soft Materials (FUNSOM), Jiangsu Key Laboratory for Carbon-Based Functional Materials and Devices, Soochow University, Suzhou 215123, Jiangsu (P. R. China)*

***Corresponding author:** zhiyao.duan@nwpu.edu.cn (Z.D.), fxzhang@dicp.ac.cn (F.Z.)*

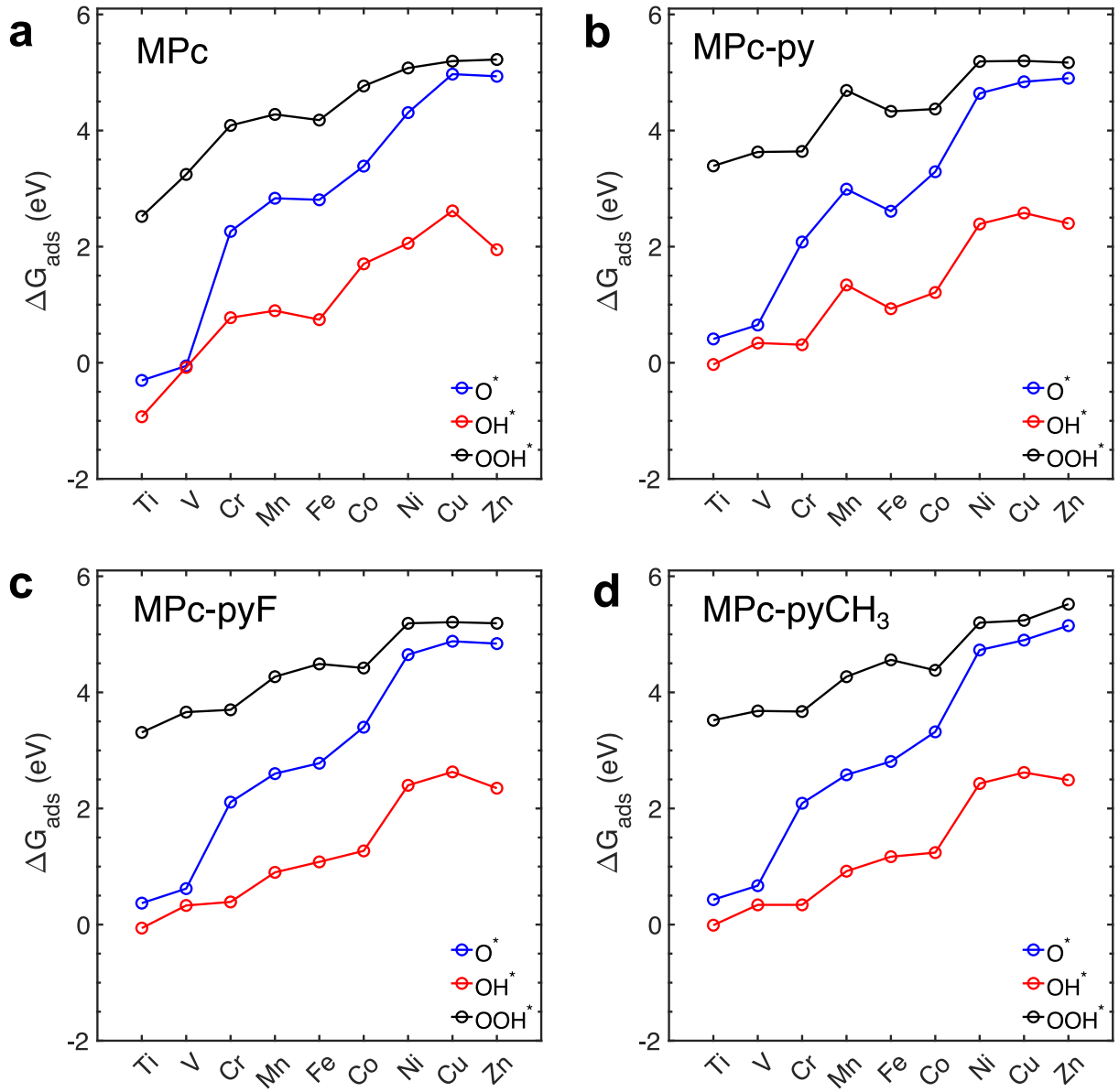


**Supplementary Fig. 1.** Calculated free energies of adsorption of ORR intermediates on **a,** MPc, **b,** M HSACs, **c,** M HSACs-F, **d,** M HSACs-$CH_3$ (M = Ti, V, Cr, Mn, Fe, Co, Ni, Cu, Zn). Source data are provided as a Source Data file.

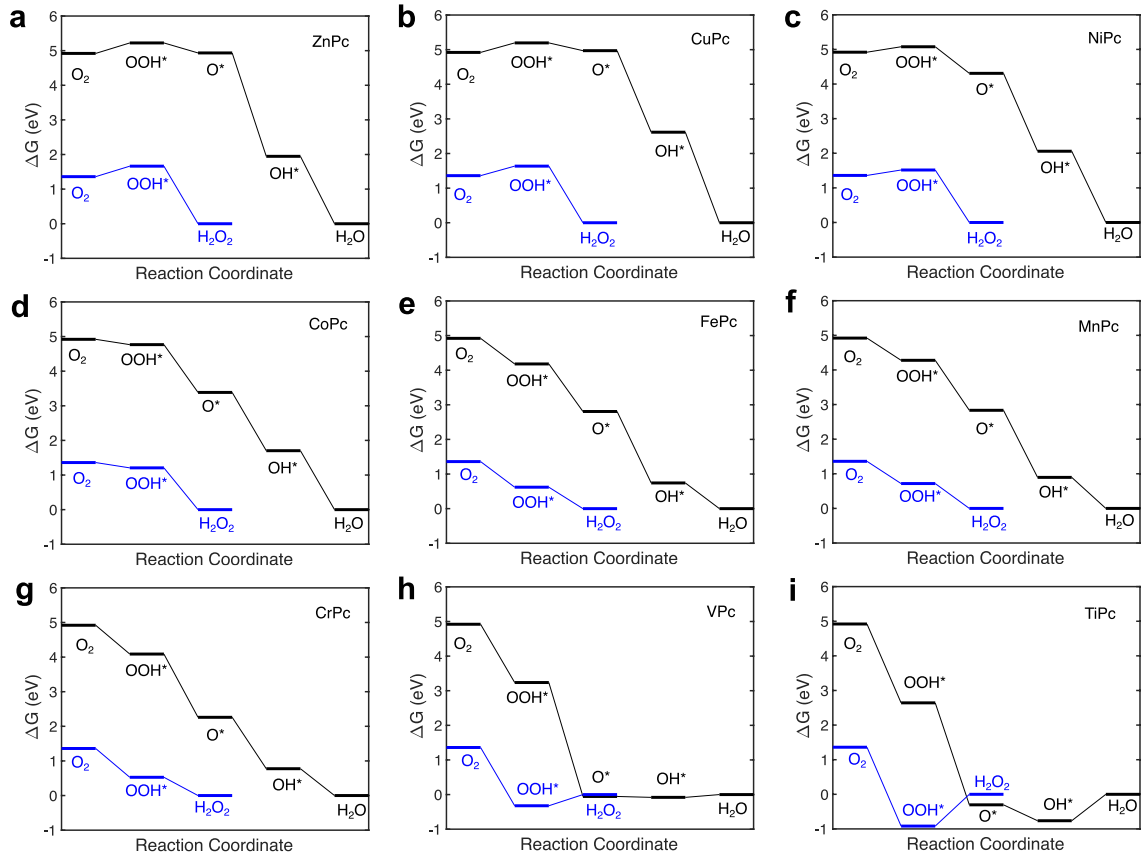


**Supplementary Fig. 2.** Calculated reaction free energy diagrams of ORR to $H_2O_2$ (blue) and water (black) on MPc at U = 0 $V_{RHE}$ (M = Ti, V, Cr, Mn, Fe, Co, Ni, Cu, Zn). Source data are provided as a Source Data file.

Apparently, MnPc favors the O-OH bond splitting for full ORR over the $H_2O_2$ production due to the lower free change of the former. On the contrary, CoPc has a $\Delta G_{OOH*}$ slightly weaker than 4.6 eV, thus the ORR reaction should proceed via the $2e^-$ reduction pathway. Interestingly, the optimal activity for the $H_2O_2$ production is predicted to occur at $\Delta G_{OOH*}$~4.2 eV by the volcano plot (see Figure 1c). But if we further consider the energetics of the competing step for the optimal selectivity as discussed above, the $\Delta G_{OOH*}$ needs to be further destabilized to about 4.6 eV in order to make $H_2O_2$ production thermodynamically favorable than the competing O* generation step. In this regard, CoPc should have the highest selectivity for the $H_2O_2$ production while still maintain appreciable ORR activity among all MPc catalysts studied.

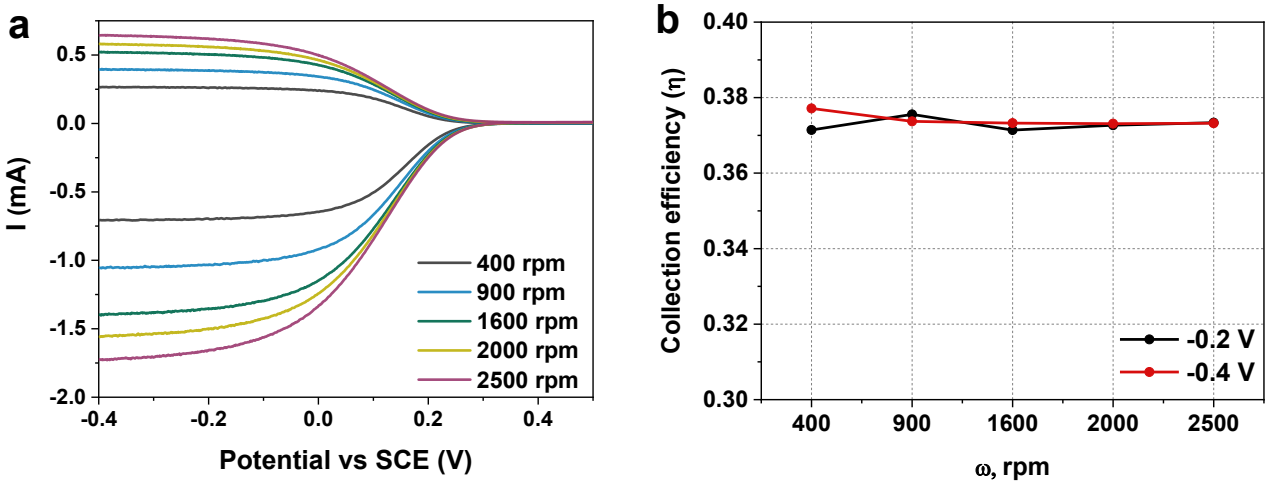


**Supplementary Fig. 3. Determination of correction efficiency of RRDE with $K_3Fe[CN]_6$.** LSVs of a Ar-saturated aqueous solution of $K_3Fe[CN]_6$ (10 mmol $L^{-1}$) in the presence of $KNO_3$ (0.1 M) recorded at a rotating-ring (Pt) and disk (GC) electrode. (a) RRDE voltammograms. The disk potential was scanned at 10 mV $s^{-1}$ and the ring potential was constant at 0.9 V vs SCE. (b) Plots of collection efficiency at -0.2 V and -0.4V vs rotation rates. Source data are provided as a Source Data file.

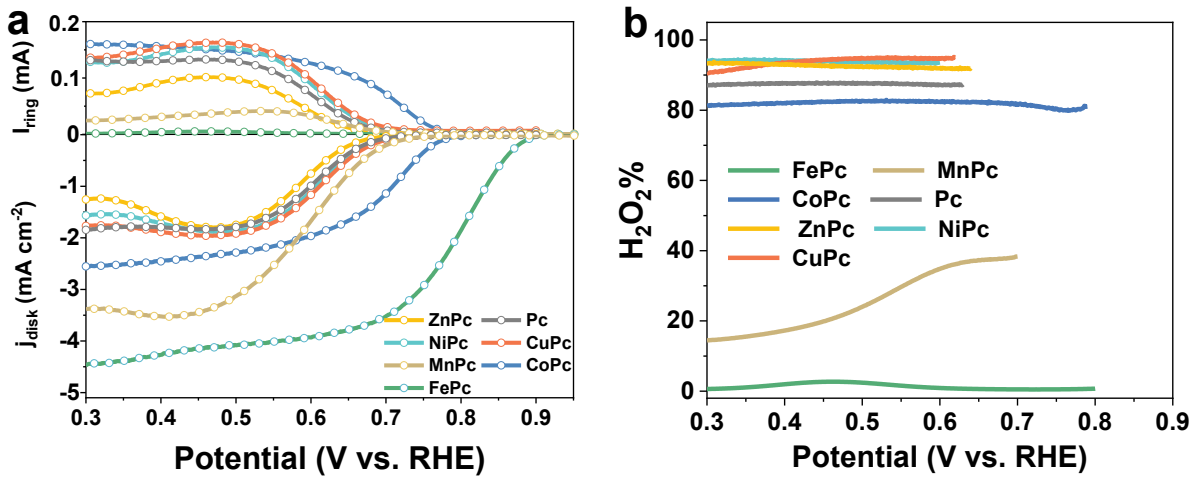


**Supplementary Fig. 4. Electrochemical 2e$^-$ ORR performance of various MPc. a,** RRDE voltammograms of MPc in $O_2$-saturated solution in 0.1 M KOH, showing the disk current density ($j_{disk}$) and ring current ($i_{ring}$). **b,** Calculated $H_2O_2$ selectivity ($H_2O_2$%) as a function of applied potential. Source data are provided as a Source Data file.

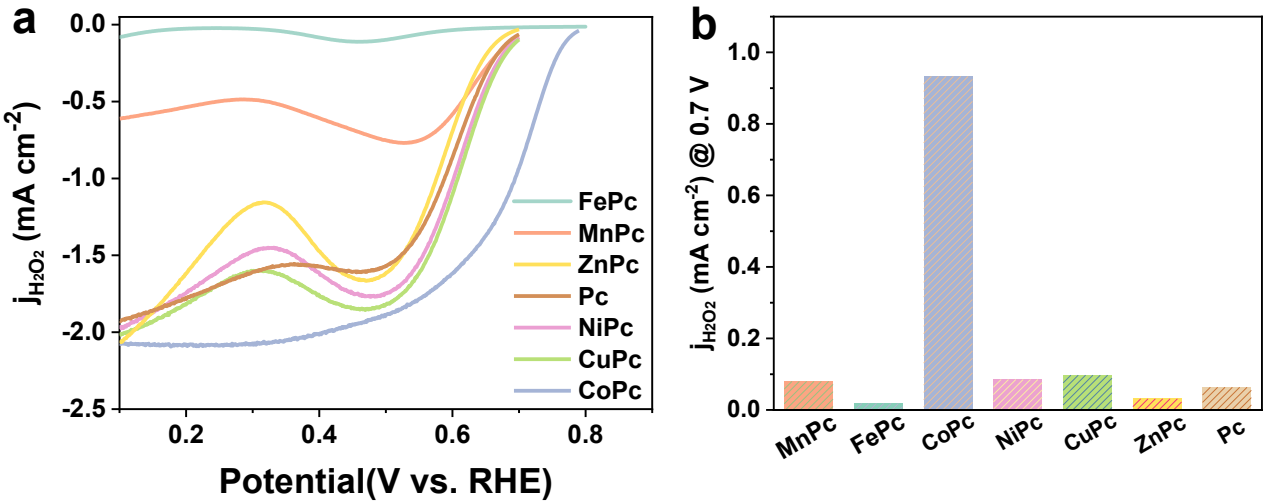


**Supplementary Fig. 5. a,** Partial current density for $H_2O_2$ production on various MPc obtained from the ring current in Supplementary Fig. 4a. **b,** Comparison of $H_2O_2$ partial current densities at 0.7 V for MPc. Source data are provided as a Source Data file.

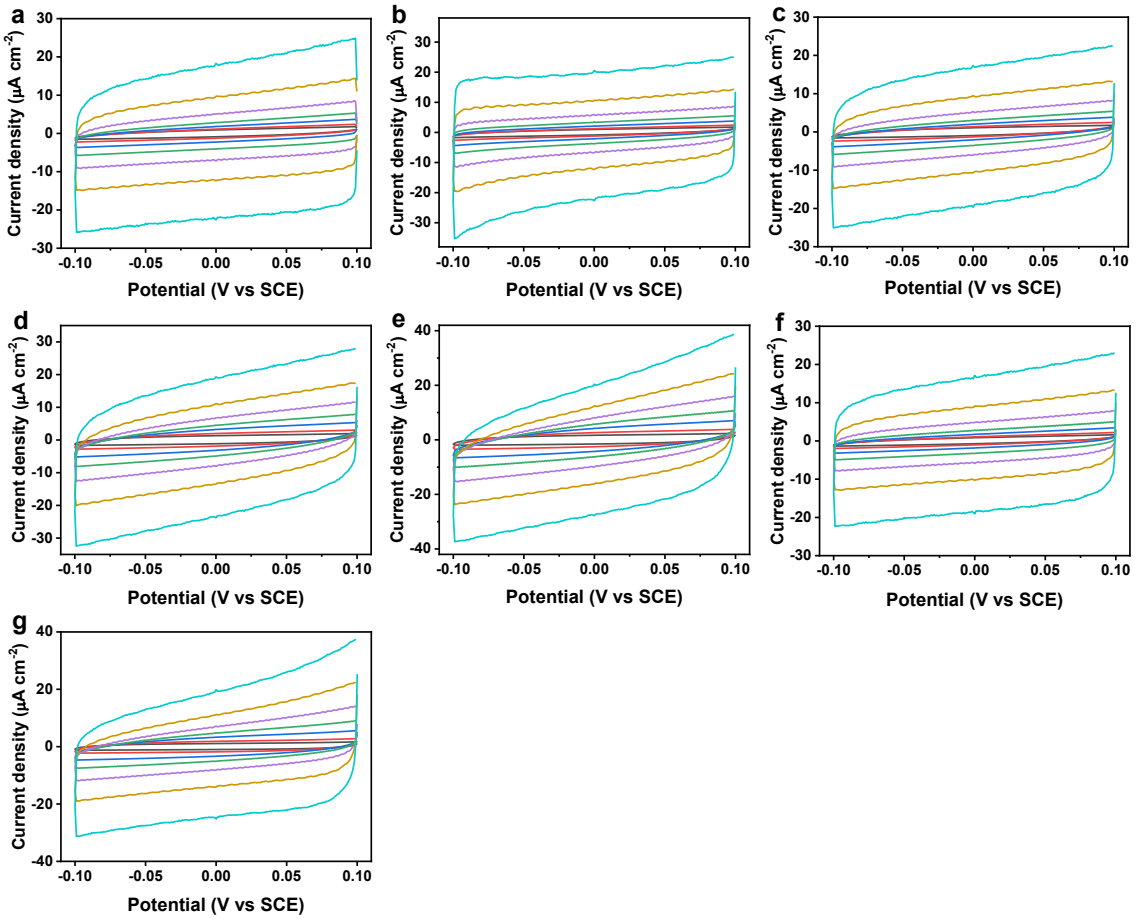


**Supplementary Fig. 6. Double-layer capacitance measurements for determining electrochemically active surface area for the MPc and Pc from voltammetry in 0.1 M KOH.** Cyclic voltammograms were measured in a non-Faradaic region of the voltammogram at the following scan rate: decrease in the order 0.8, 0.4, 0.2, 0.1, 0.05, 0.02, and 0.01 V/s. The working electrode was held at each potential vertex for 10 s before the beginning of the next sweep. All current is assumed to be due to capacitive charging. **a,** MnPc, **b,** FePc, **c,** CoPc, **d,** NiPc, **e,** CuPc, **f,** ZnPc, **g,** Pc. Source data are provided as a Source Data file.

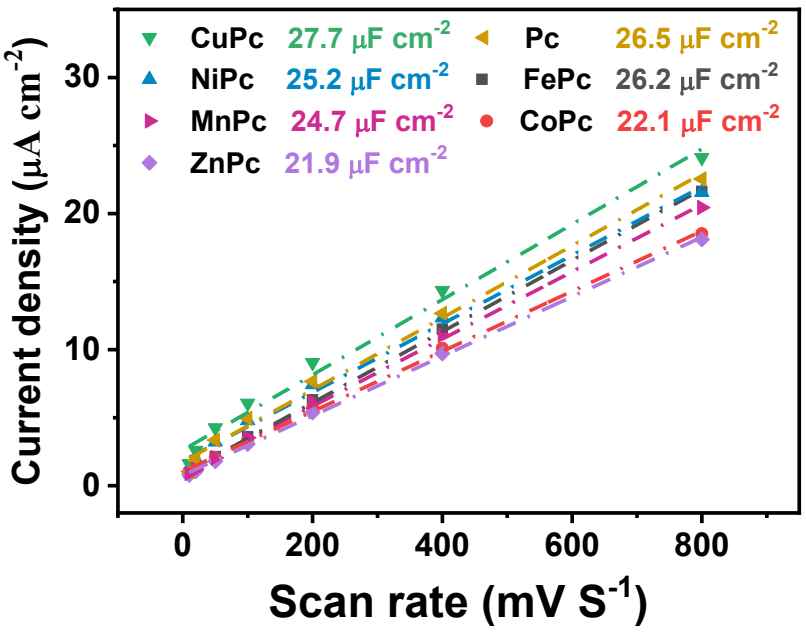


**Supplementary Fig. 7. Double-layer capacitance for the MPc and Pc from cyclic voltammetry in Supplementary Fig. 6.** The cathodic and anodic charging currents measured at 0.0 V vs SCE were plotted as a function of scan rate. Source data are provided as a Source Data file.

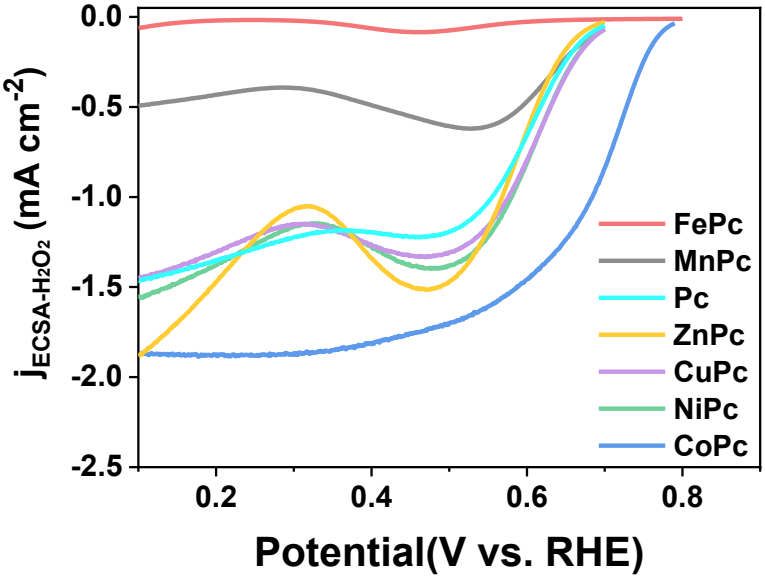


**Supplementary Fig. 8.** The ECSA-normalized current density for $H_2O_2$ production on MPc in $O_2$-saturated 0.1 M KOH solution, rotation speed 1600 rpm. Source data are provided as a Source Data file.

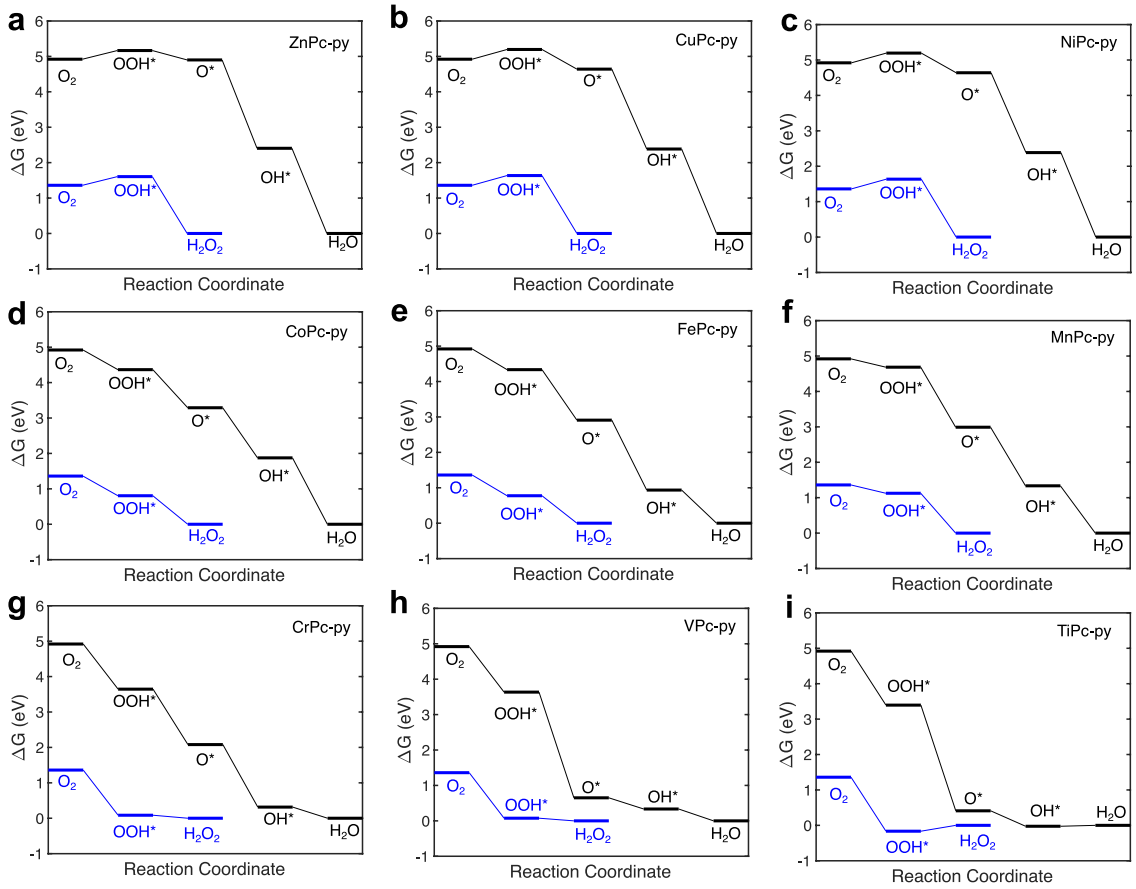


**Supplementary Fig. 9.** Calculated reaction free energy diagrams of ORR to $H_2O_2$ (blue) and water (black) on M HSACs at U = 0 $V_{RHE}$ (M = Ti, V, Cr, Mn, Fe, Co, Ni, Cu, Zn). Source data are provided as a Source Data file.

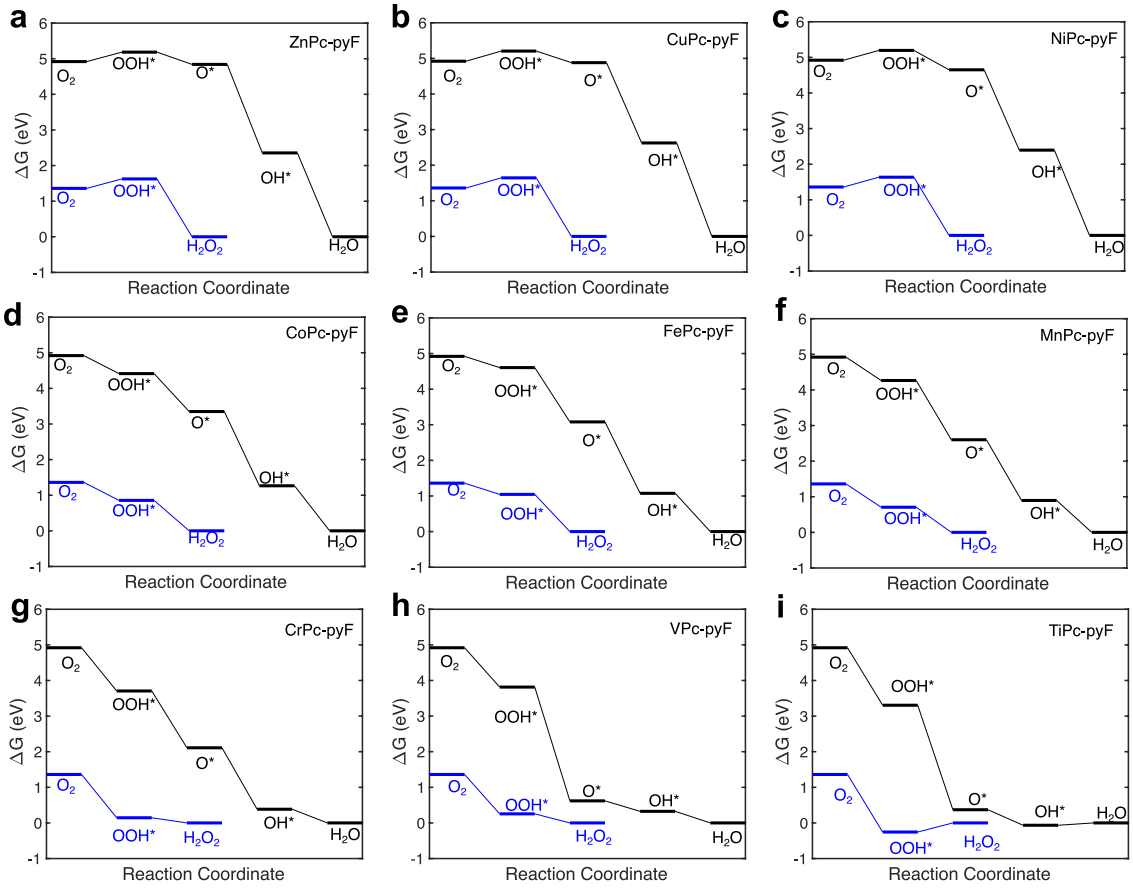


**Supplementary Fig. 10.** Calculated reaction free energy diagrams of ORR to $H_2O_2$ (blue) and water (black) on M HSACs-F at U = 0 $V_{RHE}$ (M = Ti, V, Cr, Mn, Fe, Co, Ni, Cu, Zn). Source data are provided as a Source Data file.

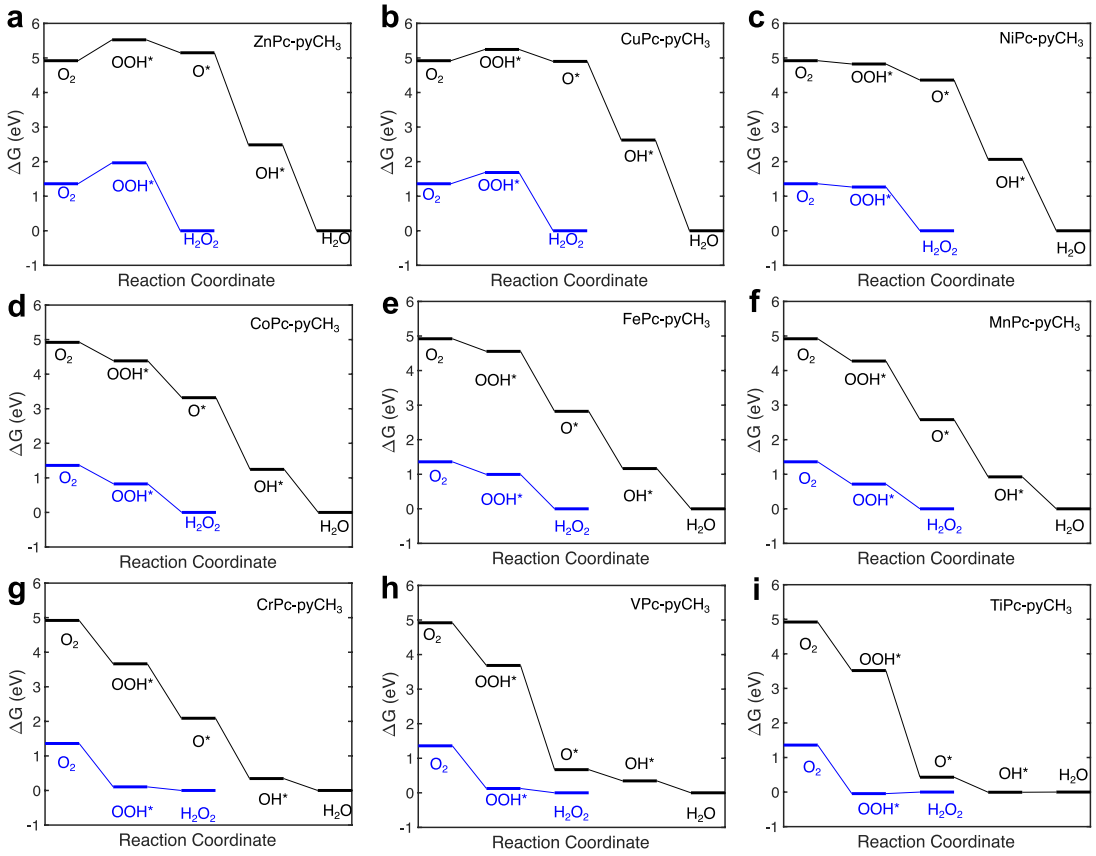


**Supplementary Fig. 11.** Calculated reaction free energy diagrams of ORR to $H_2O_2$ (blue) and water (black) on M HSACs-$CH_3$ at U = 0 $V_{RHE}$ (M = Ti, V, Cr, Mn, Fe, Co, Ni, Cu, Zn). Source data are provided as a Source Data file.

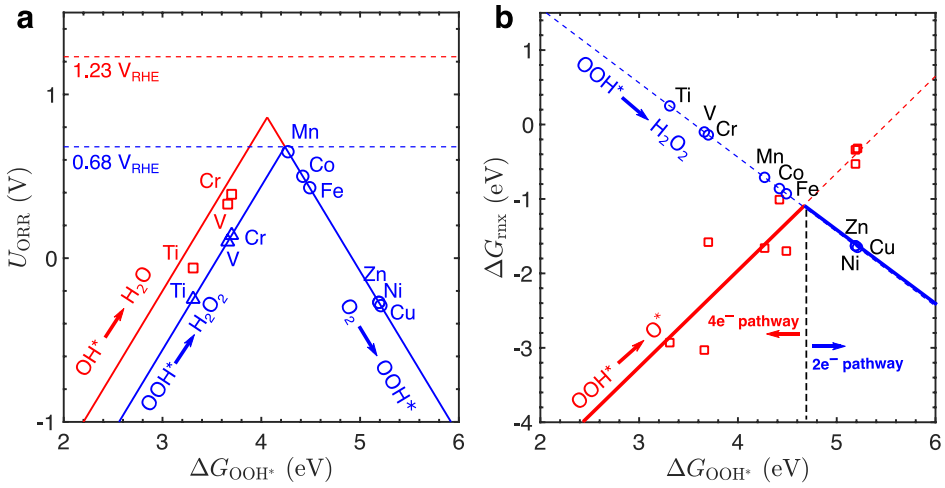


**Supplementary Fig. 12. a,** Calculated catalytic activity volcano plot for the $2e^-$ and $4e^-$ reaction pathways of ORR over M HSACs-F. **b,** Calculated selectivity plot of ORR over M HSACs-F (M = Ti, V, Cr, Mn, Fe, Co, Ni, Cu, Zn). Source data are provided as a Source Data file.

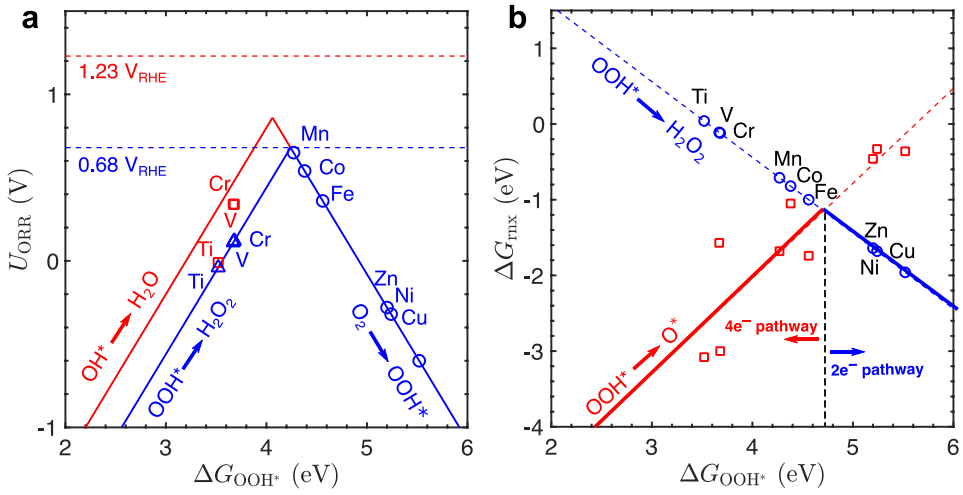


**Supplementary Fig. 13. a,** Calculated catalytic activity volcano plot for the 2e$^-$ and 4e$^-$ reaction pathways of ORR over M HSACs-CH$_3$. **b,** Calculated selectivity plot of ORR over M HSACs-CH$_3$ (M = Ti, V, Cr, Mn, Fe, Co, Ni, Cu, Zn). Source data are provided as a Source Data file.

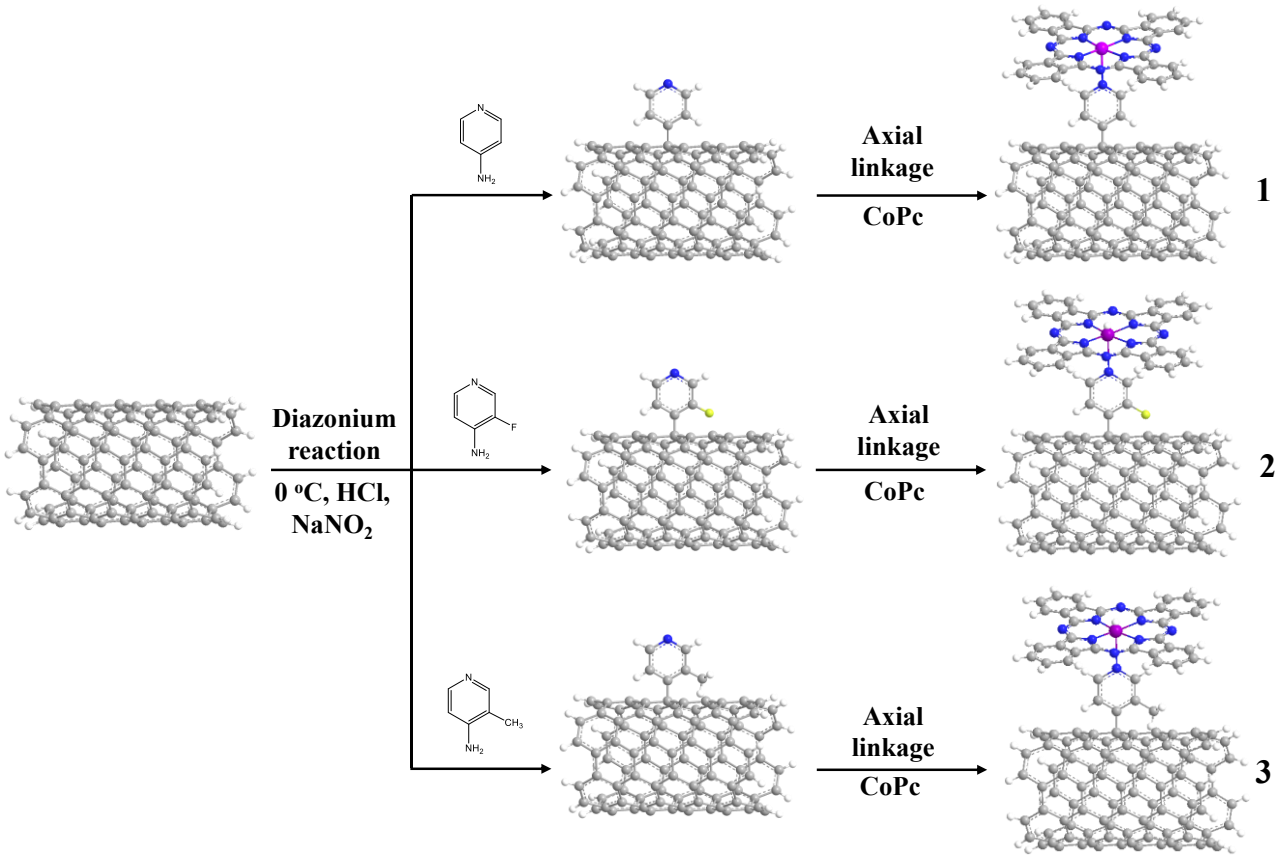


**Supplementary Fig. 14. The schematic diagram for the synthesis of heterogenized CoPc catalyst with CNT as support.** 1: Co HSACs; 2: Co HSACs-F; 3: Co HSACs-$CH_3$. Firstly, CNT was functionalized with aminopyridine by the diazonium reaction. Afterward, CoPc is axially coordinated on CNT through the metal-ligand bond between Co and N.

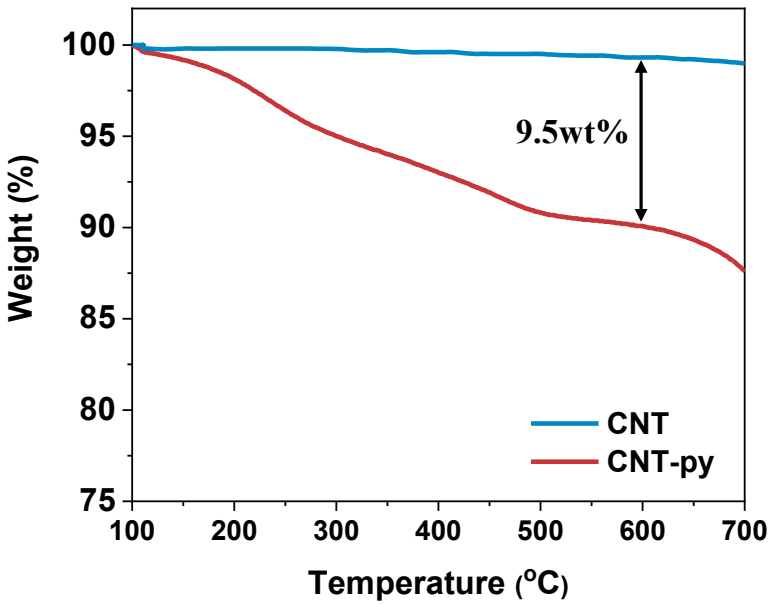


**Supplementary Fig. 15.** TGA data (10 °C $min^{-1}$) of purified CNT and pyridine-functionalized CNT (CNT-py). Source data are provided as a Source Data file.

Note:

The covalent functionalization of CNT by pyridine group was examined by TGA analysis, which showed a weight loss of 9.5 wt% at 600 °C compared to nearly no change for the purified CNT. This corresponds to ca.1 functional group for every 60 nanotube carbon atoms.

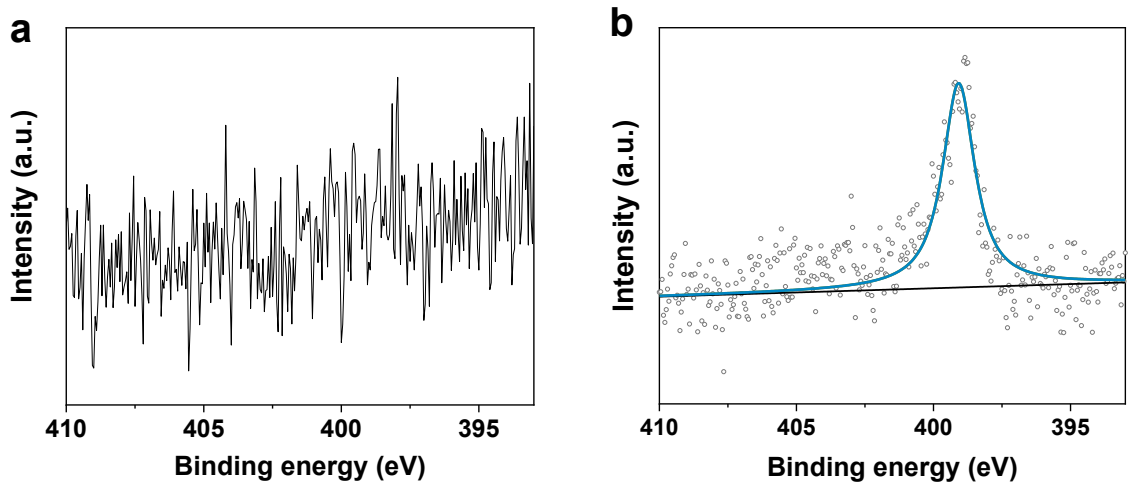


**Supplementary Fig. 16. N1*s* XPS spectra. a,** CNT. **b,** pyridine-functionalized CNT (CNT-py). The bare CNT shows no N1*s* signal, while CNT-pyridine exhibits a significant N1*s* peak ascribing to pyridine N at ca.399 eV. Source data are provided as a Source Data file.

Note:

The functionalization of CNT with pyridine group was further confirmed by XPS measurements, where elemental composition analysis exhibited the presence of ca. 1.5 at% of N in CNT-py (Supplementary Table 6), in agreement with the TGA data.

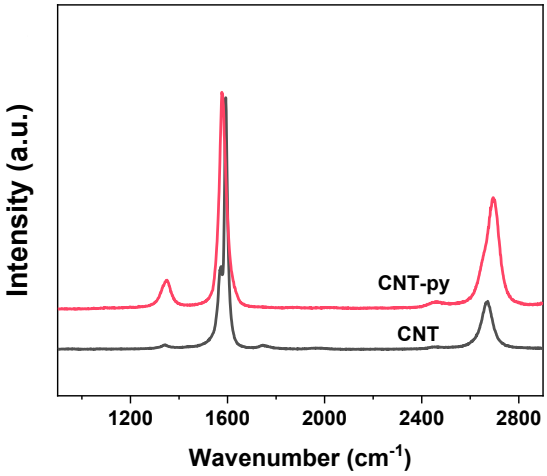


**Supplementary Fig. 17.** Raman spectra (532 nm) of purified CNT and pyridine-functionalized CNT (CNT-py) normalized at the G-band. Source data are provided as a Source Data file.

Note:

Generally, the D band accounts for the presence of defects and the G band represent the graphitic order. The Raman spectra of CNT-py exhibits an enhanced D band at ca. 1330 $cm^{-1}$ compared with that of the pure CNT, indicative of groups attached to the surface of the nanotubes.

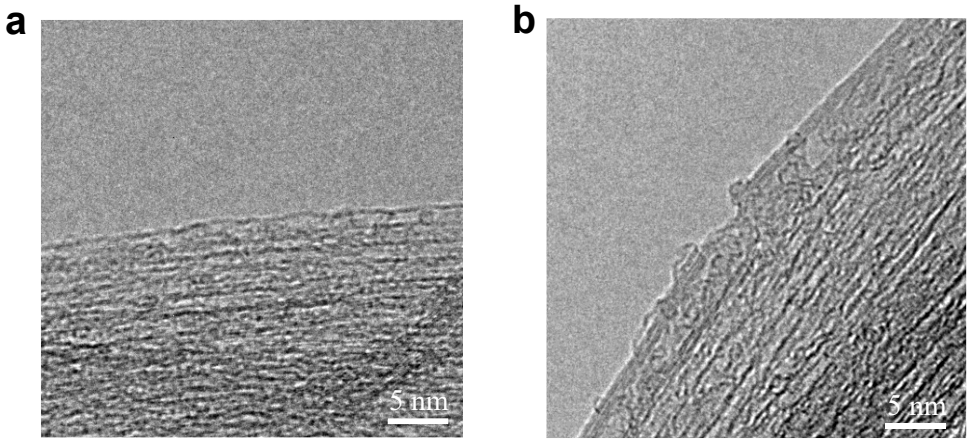


**Supplementary Fig. 18. HRTEM characterization. a,** CNT. **b,** Co HSACs. Source data are provided as a Source Data file.

Note:

The HRTEM image in Supplementary Fig.18b shows surface bumps along the sidewalls of CNT, which is the evidence of covalently functionalized moieties of pyridine group attached to CNT.

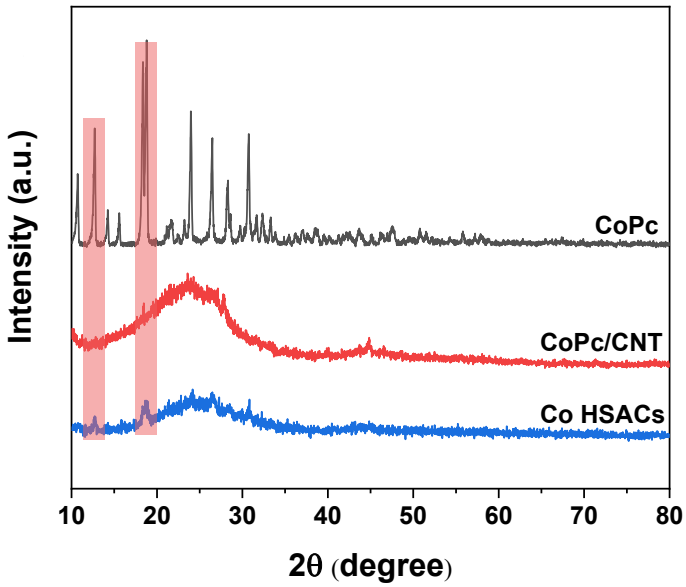


**Supplementary Fig. 19.** XRD patterns of the CoPc, CoPc/CNT, and the Co HSACs. Source data are provided as a Source Data file.

Note: XRD patterns reveal both Co HSACs and CoPc/CNT are comprised of carbon and CoPc.

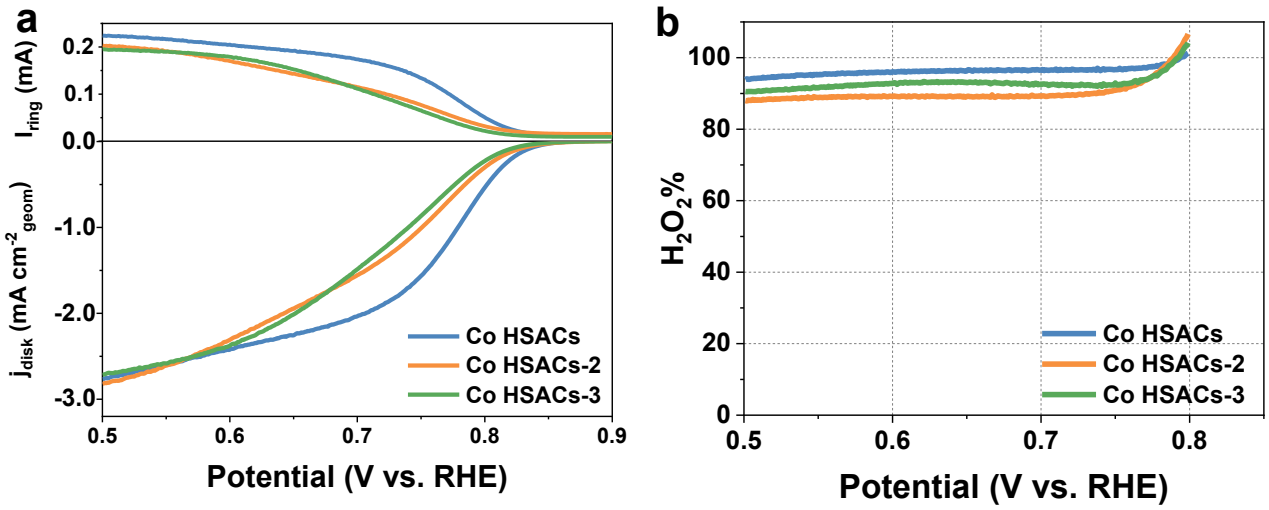


**Supplementary Fig. 20. Optimization of the content of CoPc in the Co HSACs. a,** Comparison of $2e^-$ ORR performance at 1600 rpm and the simultaneous $H_2O_2$ detection current densities at the ring electrode for Co HSACs, Co HSACs-2, and Co HSACs-3 in 0.1 KOH. **c,** The calculated $H_2O_2$ selectivity as a function of the applied potential. The contents of Co in Co HSACs, Co HSACs-2, and Co HSACs-3 are 0.7at%, 1.4 at%, and 2.1at%, respectively. Source data are provided as a Source Data file.

Note:

Considering that the N content which corresponds to the pyridinic group on the CNT is 1.43 at% by XPS (Supplementary Table 6), we have examined the effect of pyridine group content in the CNT-py using three different values, i.e., 0.7 at%, 1.4 at%, and 2.1 at% to determine the optimal loading of CoPc in the HSACs. For simplicity, the three samples with different additive amount of CoPc were denoted as Co HSACs, Co HSACs-1, and Co HSACs-2, respectively. As shown in Supplementary Fig. 20, the Co HSACs delivers higher $2e^-$ activity with more positive onset potential (Supplementary Fig. 20a) as well as better $2e^-$ selectivity (Supplementary Fig. 20b) than the other two samples. Although the Co HSACs with CoPc loading of 1.4 at% and 2.1 at% are higher than the 0.7 at% one, the excess CoPc may not coordinate with the CNT-py via the pyridinic group, due to the number of effective coordination sites and steric effect. As a result, only the coordinated CoPc could prominently enhance the $2e^-$ performance. Owing to the superior $2e^-$ performance of Co HSACs, we thus chose the 0.7 at% content of CoPc for the discussion in our manuscript.

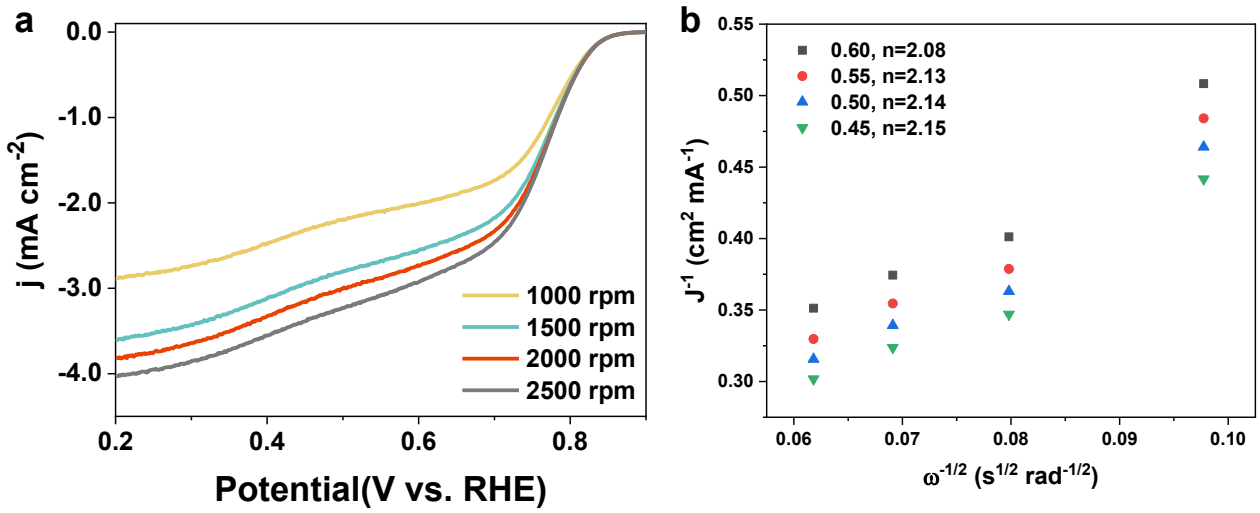


**Supplementary Fig. 21. a,** J-V curve of Co HSACs electrode measured in $O_2$-saturated with different rotating rates. **b,** K-L plots at different potentials calculated from the LSVs with different rotating rates. Source data are provided as a Source Data file.

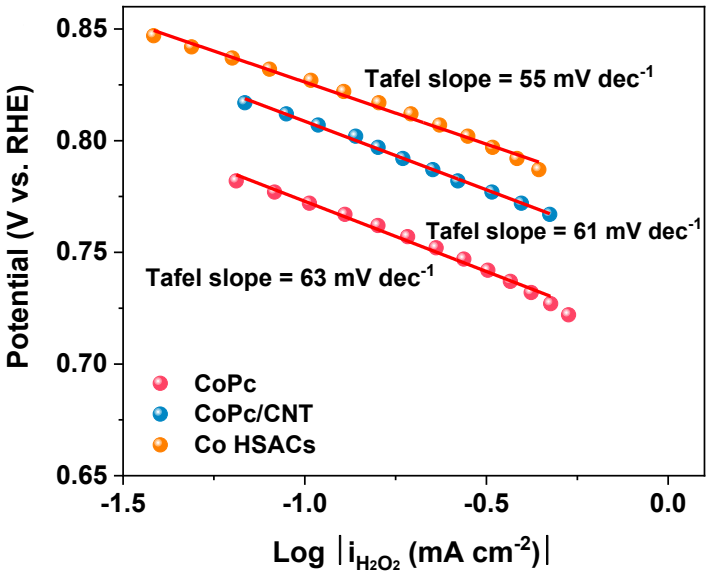


**Supplementary Fig. 22.** Tafel plots of the typical samples. Source data are provided as a Source Data file.

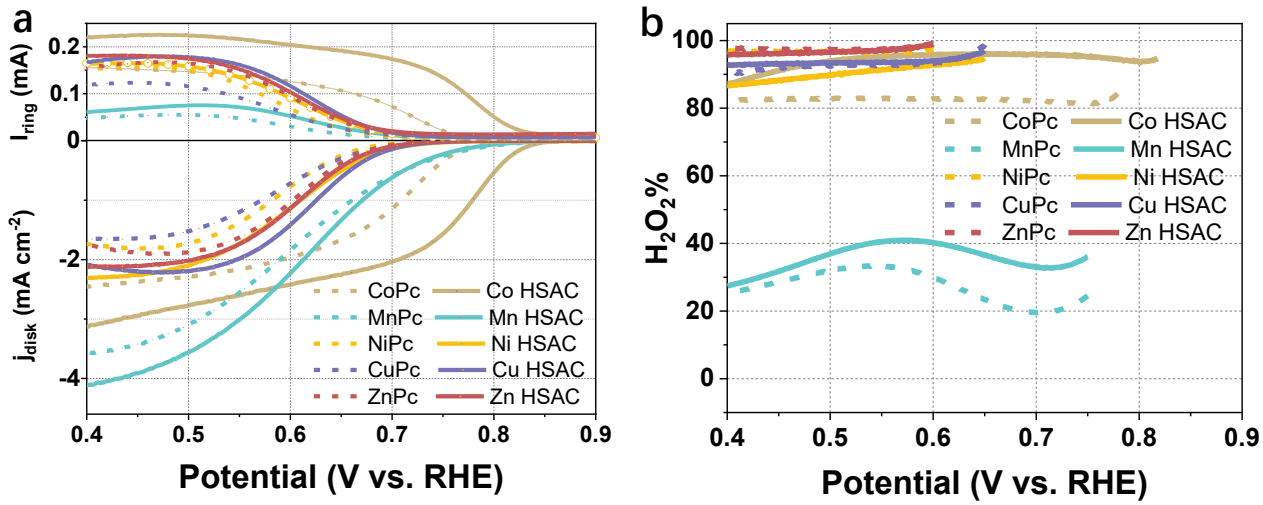


**Supplementary Fig. 23. Electrochemical 2e$^-$ ORR performance of various MPc and M HSACs.** **a,** RRDE voltammograms of MPc and M HSACs in $O_2$-saturated solution in 0.1 M KOH, showing the disk current density ($j_{disk}$) and ring current ($i_{ring}$). **b,** Calculated $H_2O_2$ selectivity ($H_2O_2$%) as a function of applied potential. Source data are provided as a Source Data file.

Note:

We prepared a series of M HSACs (M = Mn, Ni, Fe, and Zn) besides Co HSACs using the similar synthesis protocol to that of the Co HSACs. As shown in Supplementary Fig. 23, all the M HSACs show higher ORR activities as compared with the MPc. Furthermore, the 2e$^-$ selectivities of M HSACs are maintained as compared with those of the MPc counterparts (Figure Supplementary Fig. 23b), indicating the general applicability by heterogenization of the MPc to generate the HSACs for enhanced ORR performance and the capability of generating $H_2O_2$ is anticipated to increase on the M HSACs.

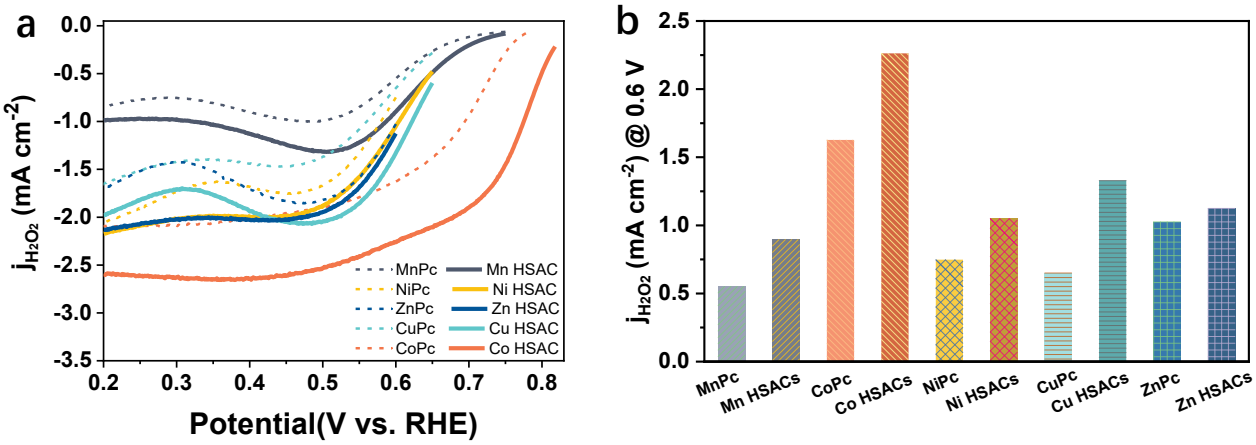


**Supplementary Fig. 24. a,** Partial current density for $H_2O_2$ production on various MPc and M HSACs obtained from the ring current in Figure R5. **b,** Comparison of $H_2O_2$ partial current densities at 0.6 V for MPc and M HSACs. Source data are provided as a Source Data file.

Note:

To prove whether the Mn-, Zn-, Ni-, and Cu-based HSACs are better catalysts for $H_2O_2$ production with high selectivity and compensated activity, we further calculated the partial current densities for $H_2O_2$ ($j_{H_2O_2}$) on various M HSACs for $H_2O_2$ production from the ring current. As shown in Supplementary Fig. 24, the Co HSACs exhibits a much earlier onset potential for $H_2O_2$ generation and its $j_{H_2O_2}$ is prominently higher than other samples across the whole range of potential windows. Specially, the $j_{H_2O_2}$ on Co HSACs at 0.6 V is ca. 2.3 mA $cm^{-2}$, which is 1.4 times, 2.6 times, 2.5 times, 1.7 times, and 2.0 times as those of CoPc, Mn HSACs, Ni HSACs, Cu HSACs, and Zn HSACs, respectively. Therefore, it is reasonable to conclude that the Co HSACs could deliver the best $H_2O_2$ production ability, although the Cu-, Ni-, and Zn-based HSACs also exhibit high selectivity for $H_2O_2$ production.

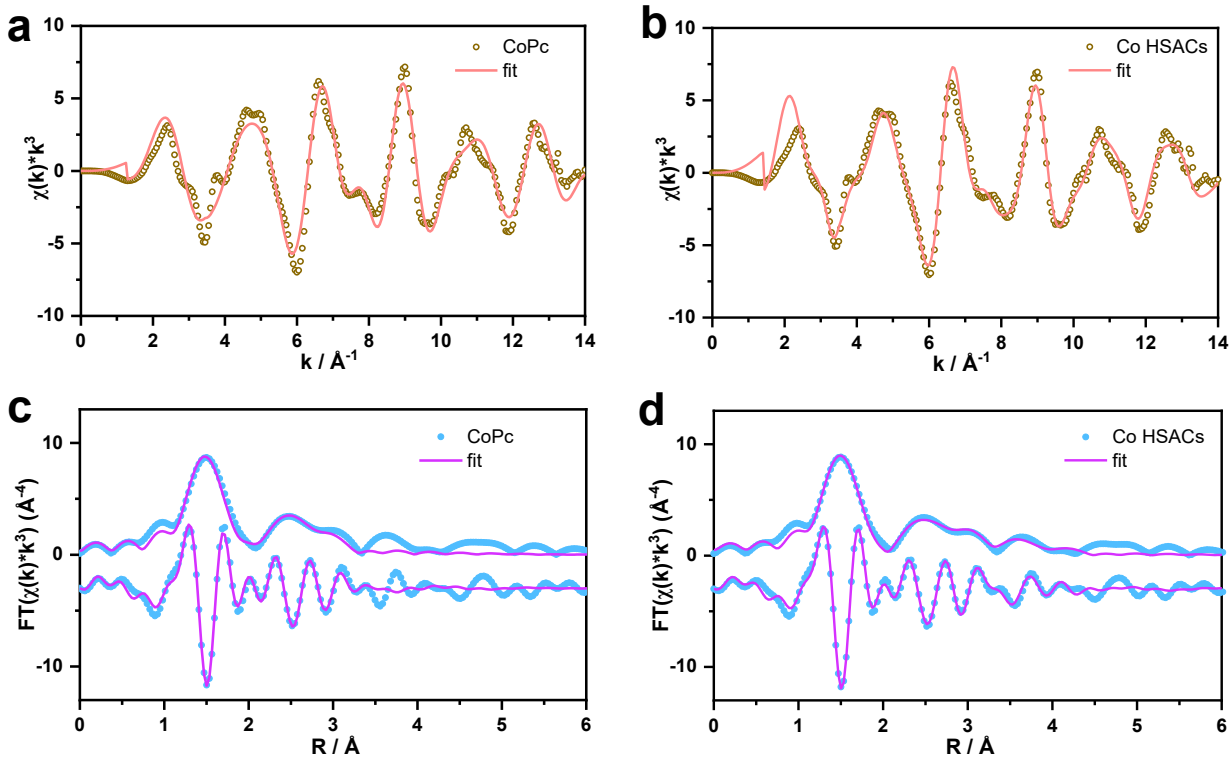


**Supplementary Fig. 25. Fitting curves of the FT-EXAFS spectra for CoPc and Co HSACs: a-b,** at K space. **c-d,** at R space. Source data are provided as a Source Data file.

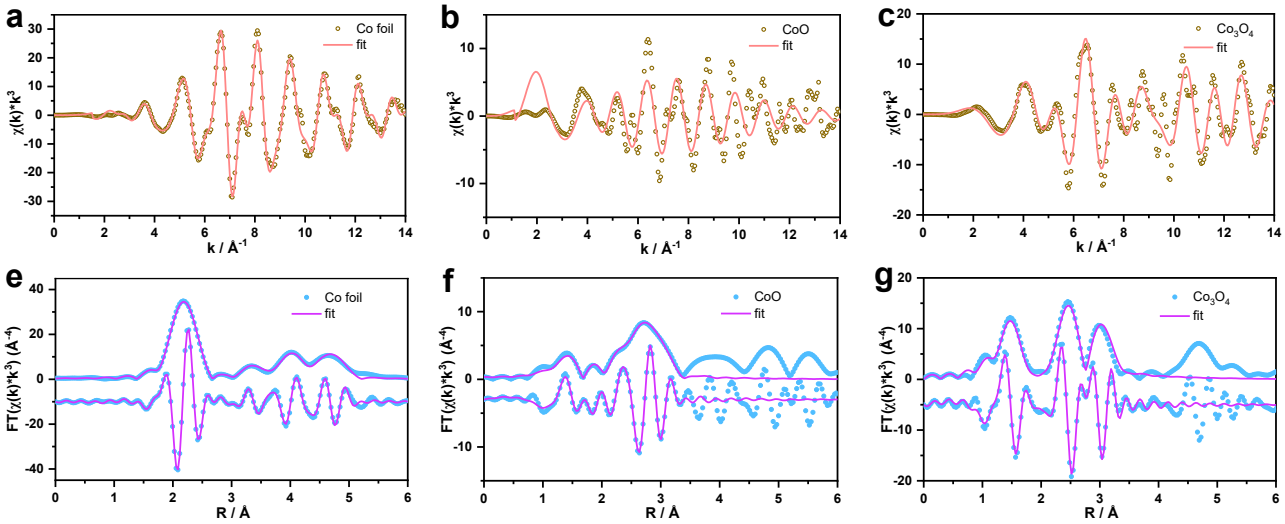


**Supplementary Fig. 26. Fitting curves of the FT-EXAFS spectra for Co foil, CoO, and $Co_3O_4$: a-c,** at K space. **c-d,** at R space. Source data are provided as a Source Data file.

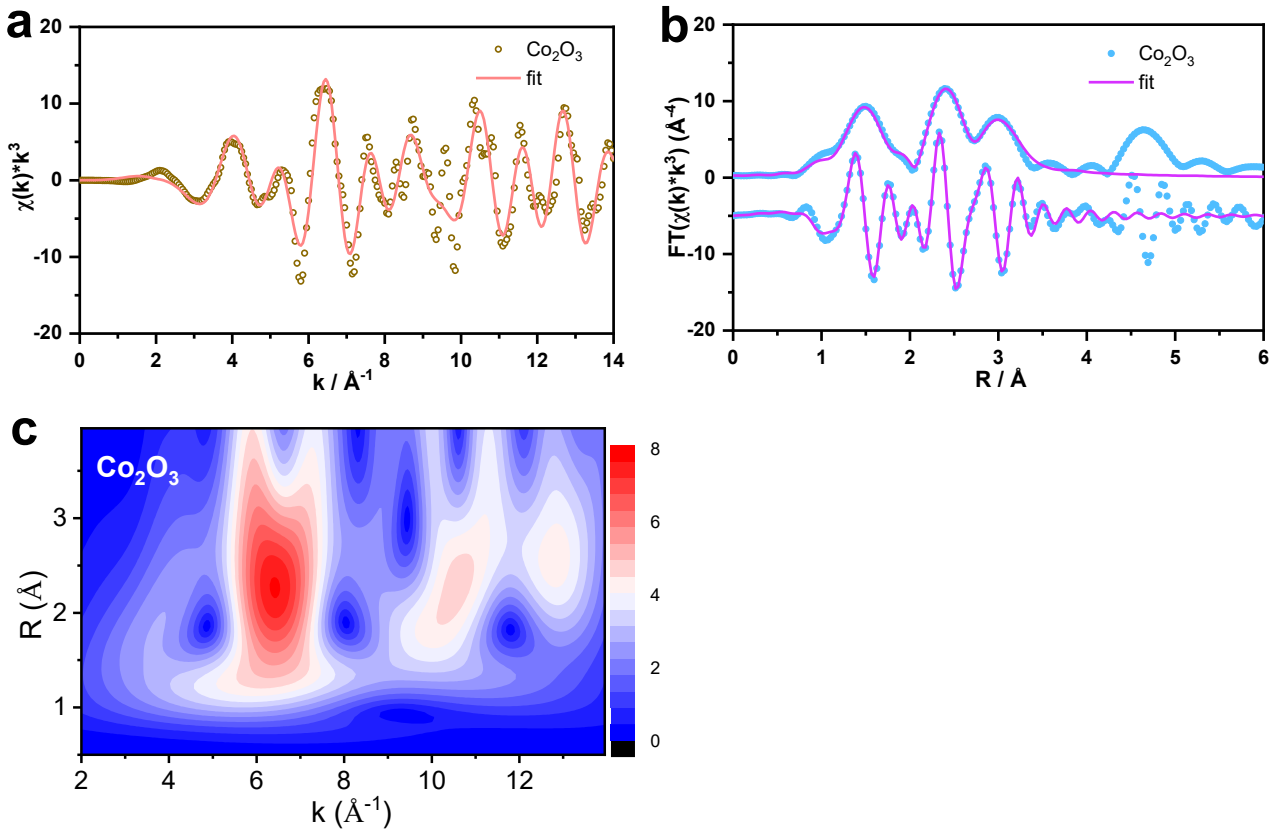


**Supplementary Fig. 27. Fitting curves of the FT-EXAFS spectra for $Co_2O_3$: a,** at K space. **b,** at R space. **c,** wavelet transform for the $k^3$-weighted EXAFS signals. Source data are provided as a Source Data file.

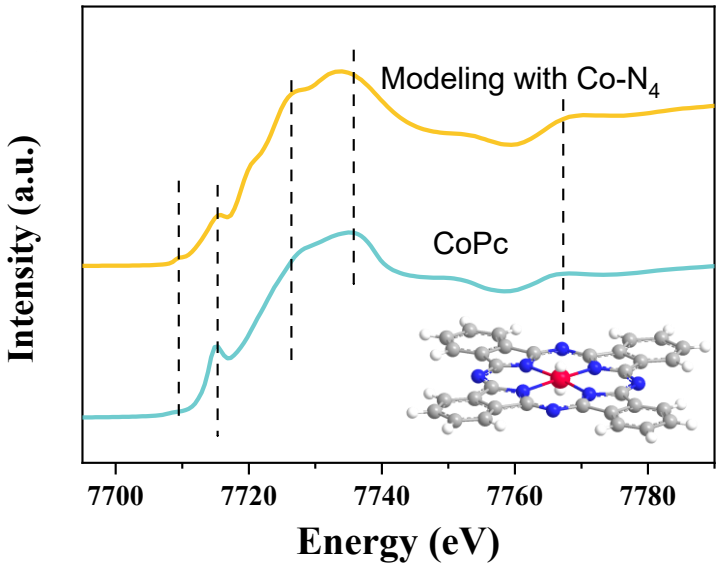


**Supplementary Fig. 28.** Comparison between the Co K-edge XANES experimental spectrum and the theoretical spectrum calculated with the depicted structure (inset) for CoPc. Source data are provided as a Source Data file.

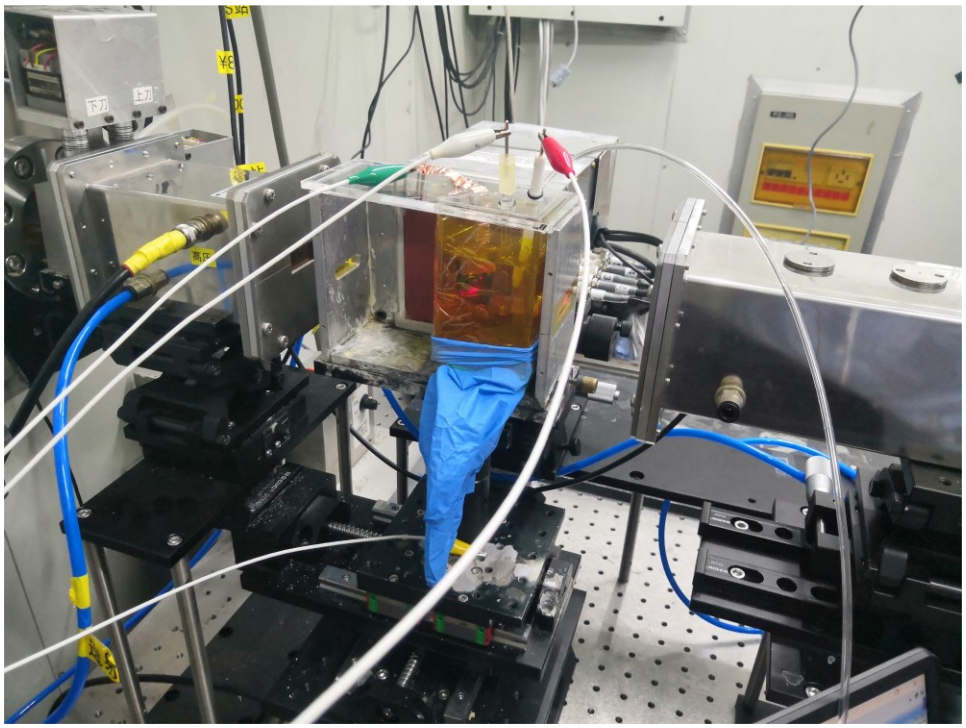

**Supplementary Fig. 29.** The operando XAS electrolyzer for electrochemical $O_2$ reduction.

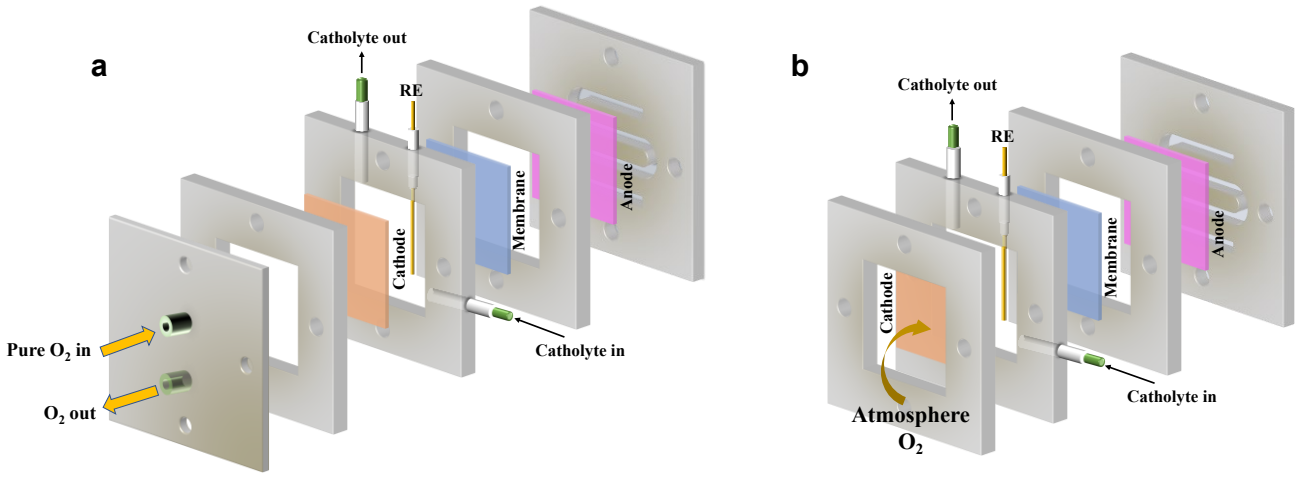


**Supplementary Fig. 30. Schematic diagram of the air-breathing flow cell configuration: a,** conventional flow cell purged with pure $O_2$ as the reactant. **b,** air-breathing flow cell with natural air diffusion electrode. Source data are provided as a Source Data file.

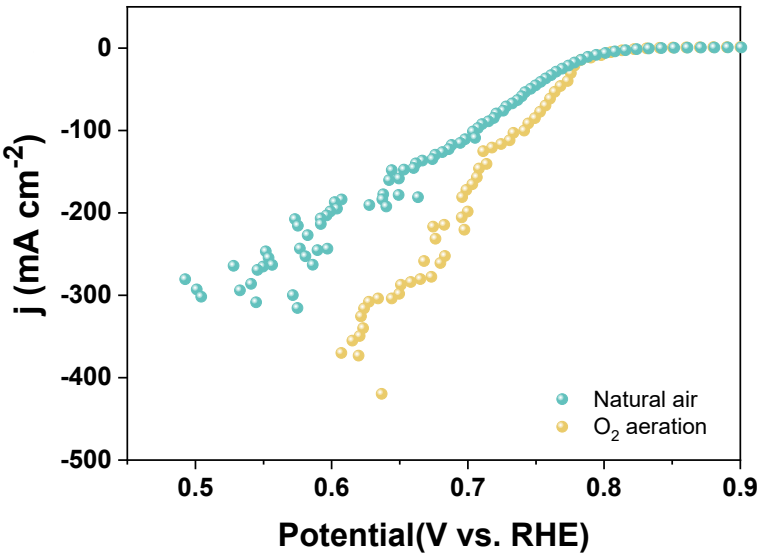


**Supplementary Fig. 31.** Comparison of the LSVs of Co HSACs in flow cell with $O_2$ aeration and air as the oxygen supply, respectively. The estimated cell voltage is ~6.5 V at 300 mA $cm^{-2}$. Source data are provided as a Source Data file.

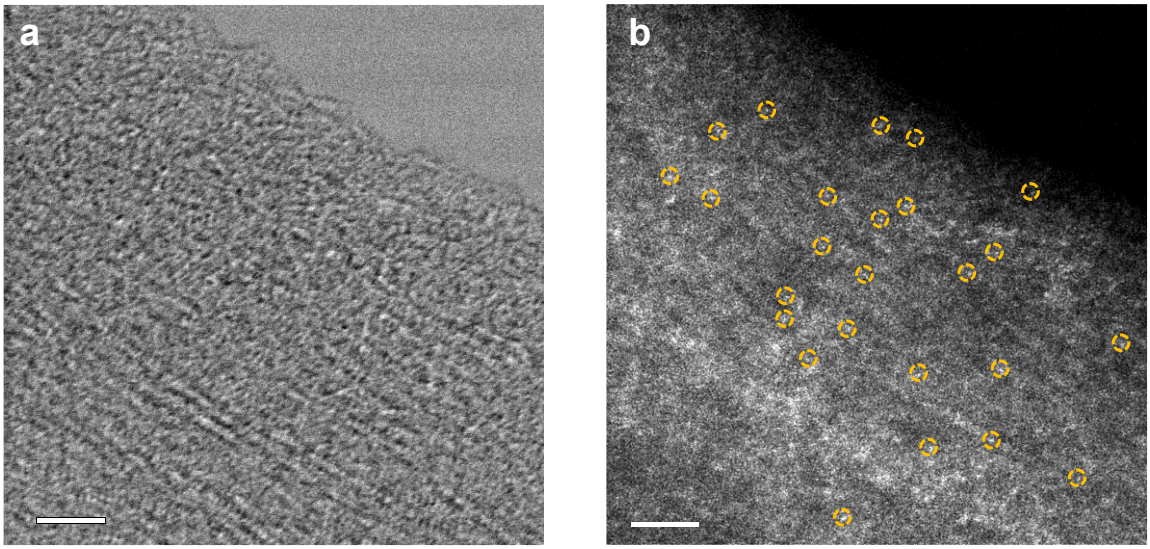


**Supplementary Fig. 32.** Aberration-corrected atomic-resolution TEM image (a) and HAADF-STEM image (b) of Co HSACs after stability test. The bright spots of Co atoms are marked with yellow circles. Source data are provided as a Source Data file.

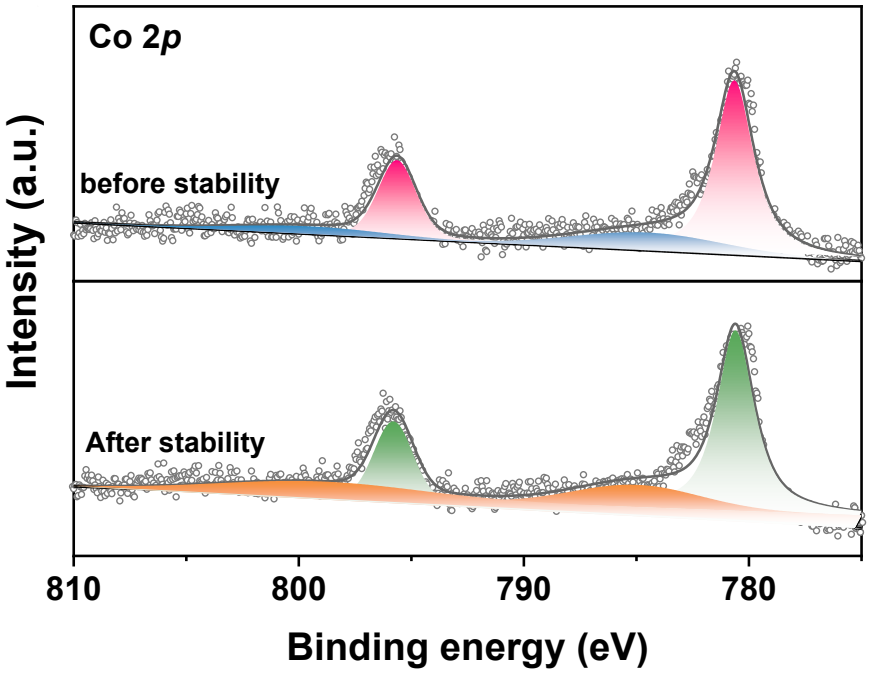


**Supplementary Fig. 33.** High-resolution XPS spectra of Co 2*p* for Co HSACs before and after the stability test. Source data are provided as a Source Data file.

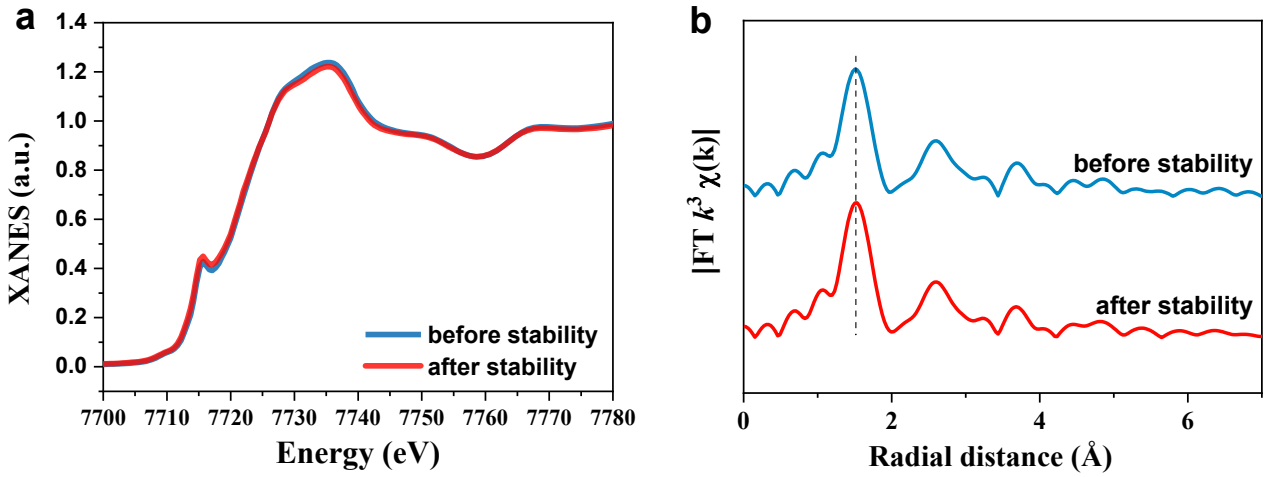


**Supplementary Fig. 34.** Comparison of the XANES and EXAFS spectra of the Co HSACs before and after stability test. Source data are provided as a Source Data file.

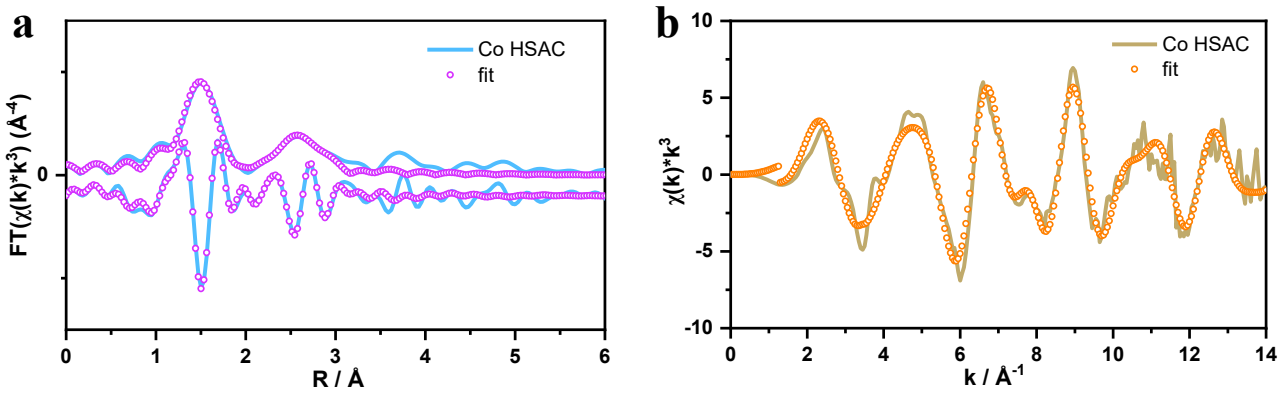


**Supplementary Fig. 35. Fitting curves of the FT-EXAFS spectra for Co HSACs after stability: a,** at R space. **b,** at K space. Source data are provided as a Source Data file.

Note:

As shown in Supplementary Fig. 31, the Co HSACs before and after stability test show nearly identical XANES spectra and EXAFS spectra. Furthermore, the coordination structure of Co-N was maintained after the stability test as displayed by the fitting curves of the FT-EXAFS shown in Supplementary Fig. 32 and Supplementary Table 9, suggesting the robustness of Co HSACs under high current density.

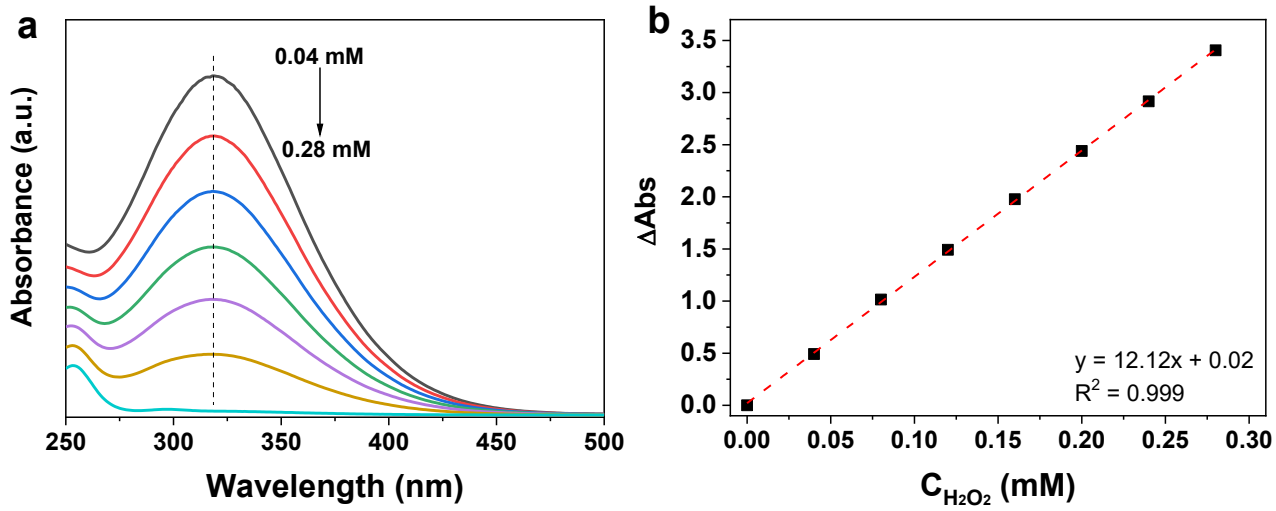


**Supplementary Fig. 36. The $H_2O_2$ concentrations in electrolytes were measured by titration using standard ceric sulfate solution, $Ce(SO_4)_2$.** (a) Absorption spectra changes of the cerium titration solution (1 mM) with the gradual addition of the $H_2O_2$ (0.04 - 0.28 mM). (b) Plot of the absorbance change at $\lambda$ = 318 nm as a function of the concentration of $H_2O_2$. Source data are provided as a Source Data file.

**Supplementary Table 1.** Total energies and adsorption energies of ORR intermediates on MPc of various spin states.

| | | LS | $\Delta E_{LS}$ | IS | $\Delta E_{IS}$ | HS | $\Delta E_{HS}$ |
|---|---|---|---|---|---|---|---|
| TiPc | slab | -420.77 | | | | | |
| | OH* | -432.79 | -1.15 | | | | |
| | O* | -428.61 | -0.34 | | | | |
| | OOH* | -437.03 | 2.12 | | | | |
| VPc | slab | | | | | -422.07 | |
| | OH* | | | | | -433.37 | -0.43 |
| | O* | | | | | -429.67 | -0.10 |
| | OOH* | | | | | -437.65 | 2.80 |
| CrPc | slab | | | | | -422.95 | |
| | OH* | | | | | -433.39 | 0.68 |
| | O* | | | | | -428.23 | 2.22 |
| | OOH* | | | | | -437.68 | 3.64 |
| MnPc | slab | | | -421.09 | | -421.58 | |
| | OH* | | | -431.00 | | -431.90 | 0.56 |
| | O* | | | | | -426.28 | 2.80 |
| | OOH* | | | -435.30 | | -436.11 | 3.84 |
| FePc | slab | | | -420.27 | | -420.02 | |
| | OH* | -429.83 | 1.31 | -430.48 | 0.66 | -430.74 | 0.40 |
| | O* | -424.58 | 3.19 | -425.00 | 2.76 | -424.92 | 2.85 |
| | OOH* | -434.31 | 4.33 | -434.71 | 3.93 | -434.90 | 3.75 |
| CoPc | slab | -419.64 | | | | | |
| | OH* | -429.15 | 1.37 | -428.43 | 2.08 | -428.27 | 2.25 |
| | O* | -423.56 | 3.58 | -423.79 | 3.35 | -423.67 | 3.47 |
| | OOH* | -433.69 | 4.32 | -432.79 | 5.22 | -432.46 | 5.56 |
| NiPc | slab | -417.18 | | | | | |
| | OH* | | | | | -426.33 | 1.73 |
| | O* | | | | | -420.41 | 4.27 |
| | OOH* | | | | | -430.91 | 4.64 |
| CuPc | slab | -416.26 | | | | | |
| | OH* | -424.86 | 2.27 | | | | |
| | O* | -418.83 | 4.93 | | | | |
| | OOH* | -429.88 | 4.75 | | | | |
| ZnPc | slab | -415.67 | | | | | |
| | OH* | -424.94 | 1.60 | | | | |
| | O* | -418.28 | 4.89 | | | | |
| | OOH* | -429.26 | 4.79 | | | | |

**Supplementary Table 2.** Electrochemical parameters for the calculation of ECSA.

| Sample | Double-layer capacitance, $C_{dl}$ (μF cm$^{-2}$) | ECSA (cm$^2$) |
|---|---|---|
| Pc | 26.5 | 0.3242 |
| MnPc | 24.7 | 0.3056 |
| FePc | 26.2 | 0.3242 |
| CoPc | 22.1 | 0.2735 |
| NiPc | 25.2 | 0.3119 |
| CuPc | 27.7 | 0.3428 |
| ZnPc | 21.9 | 0.2710 |

Based on literature precedent, the double-layer capacitance of a planar glassy carbon surface, $C_{dl\text{-}planar}$, was taken as 20 μF cm$^{-2}$.

**Supplementary Table 3.** Total energies and adsorption energies of ORR intermediates on M HSACs of various spin states (M = Ti, V, Cr, Mn, Fe, Co, Ni, Cu, Zn).

| | | $E_{LS}$/eV | $\Delta E_{LS}$/eV | $E_{IS}$/eV | $\Delta E_{IS}$/eV | $E_{HS}$/eV | $\Delta E_{HS}$/eV |
|---|---|---|---|---|---|---|---|
| TiPc-py | slab | -492.96 | | | | | |
| | OH* | -504.20 | -0.37 | | | | |
| | O* | -500.09 | 0.37 | | | | |
| | OOH* | -508.38 | 2.95 | | | | |
| VPc-py | slab | | | | | -494.27 | |
| | OH* | | | | | -505.15 | 0.00 |
| | O* | | | | | -501.16 | 0.61 |
| | OOH* | | | | | -509.45 | 3.19 |
| CrPc-py | slab | | | | | -494.46 | |
| | OH* | | | | | -505.36 | -0.03 |
| | O* | | | | | -499.92 | 2.04 |
| | OOH* | | | | | -509.63 | 3.20 |
| MnPc-py | slab | -491.86 | | -492.70 | | -493.52 | |
| | OH* | -502.46 | 1.94 | -503.00 | 1.39 | -503.40 | 1.00 |
| | O* | -497.37 | 3.65 | | | -498.07 | 2.95 |
| | OOH* | -506.71 | 5.19 | -507.28 | 4.62 | -507.65 | 4.25 |
| FePc-py | slab | -491.45 | | -491.88 | | -491.29 | |
| | OH* | -501.86 | 0.89 | -501.99 | 0.76 | -502.16 | 0.59 |
| | O* | -496.40 | 2.98 | -496.81 | 2.57 | -496.51 | 2.87 |
| | OOH* | -506.28 | 3.98 | -506.25 | 4.00 | -506.36 | 3.89 |
| CoPc-py | slab | -491.33 | | | | | |
| | OH* | -501.34 | 0.87 | -500.67 | 1.53 | -500.35 | 1.85 |
| | O* | -495.58 | 3.25 | -495.21 | 3.62 | | |
| | OOH* | -505.78 | 3.93 | -505.18 | 4.52 | -504.61 | 5.10 |
| NiPc-py | slab | -488.65 | | | | -488.98 | |
| | OH* | | | | | -497.81 | 2.05 |
| | O* | | | | | -491.88 | 4.60 |
| | OOH* | | | | | -502.60 | 4.75 |
| CuPc-py | slab | -487.70 | | | | | |
| | OH* | | | | | -496.34 | 2.24 |
| | O* | | | | | -490.40 | 4.80 |
| | OOH* | | | | | -501.31 | 4.76 |
| ZnPc-py | slab | -487.47 | | | | | |
| | OH* | -496.28 | 2.06 | | | | |
| | O* | -490.11 | 4.86 | | | | |
| | OOH* | -501.12 | 4.73 | | | | |

**Supplementary Table 4.** Total energies and adsorption energies of ORR intermediates on M HSACs-F of various spin states (M = Ti, V, Cr, Mn, Fe, Co, Ni, Cu, Zn).

| | | $E_{LS}$/eV | $\Delta E_{LS}$/eV | $E_{IS}$/eV | $\Delta E_{IS}$/eV | $E_{HS}$/eV | $\Delta E_{HS}$/eV |
|---|---|---|---|---|---|---|---|
| TiPc-pyF | slab | -493.11 | | | | | |
| | OH* | -504.39 | -0.40 | | | | |
| | O* | -500.28 | 0.33 | | | | |
| | OOH* | -508.62 | 2.87 | | | | |
| VPc-pyF | slab | | | | | -494.45 | |
| | OH* | | | | | -505.34 | -0.01 |
| | O* | | | | | -501.37 | 0.58 |
| | OOH* | | | | | -509.60 | 3.22 |
| CrPc-pyF | slab | | | | | -494.69 | |
| | OH* | | | | | -505.52 | 0.05 |
| | O* | | | | | -500.12 | 2.07 |
| | OOH* | | | | | -509.80 | 3.26 |
| MnPc-pyF | slab | -492.05 | | -492.92 | | -493.29 | |
| | OH* | -502.61 | 1.56 | -503.15 | 1.02 | -503.61 | 0.56 |
| | O* | -497.41 | 3.38 | | | -498.23 | 2.56 |
| | OOH* | -506.86 | 4.81 | -507.44 | 4.23 | -507.84 | 3.83 |
| FePc-pyF | slab | -491.62 | | -492.08 | | -492.22 | |
| | OH* | -502.02 | 1.08 | -502.19 | 0.91 | -502.36 | 0.74 |
| | O* | -496.57 | 3.15 | -496.98 | 2.74 | -496.68 | 3.03 |
| | OOH* | -506.43 | 4.16 | -506.44 | 4.15 | -506.55 | 4.05 |
| CoPc-pyF | slab | -491.55 | | | | | |
| | OH* | -501.50 | 0.93 | -500.88 | 1.55 | -500.55 | 1.88 |
| | O* | -495.74 | 3.36 | -495.42 | 3.63 | | |
| | OOH* | -505.95 | 3.98 | -505.38 | 4.55 | -504.80 | 5.13 |
| NiPc-pyF | slab | -488.83 | | | | -489.18 | |
| | OH* | | | | | -498.00 | 2.06 |
| | O* | | | | | -492.07 | 4.61 |
| | OOH* | | | | | -502.80 | 4.75 |
| CuPc-pyF | slab | -487.92 | | | | | |
| | OH* | -496.51 | 2.29 | | | | |
| | O* | -490.58 | 4.84 | | | | |
| | OOH* | -501.53 | 4.77 | | | | |
| ZnPc-pyF | slab | -487.65 | | | | | |
| | OH* | -496.51 | 2.01 | | | | |
| | O* | -490.35 | 4.80 | | | | |
| | OOH* | -501.28 | 4.75 | | | | |

**Supplementary Table 5.** Total energies and adsorption energies of ORR intermediates on M HSACs-$CH_3$ of various spin states (M = Ti, V, Cr, Mn, Fe, Co, Ni, Cu, Zn).

| | | $E_{LS}$/eV | $\Delta E_{LS}$/eV | $E_{IS}$/eV | $\Delta E_{IS}$/eV | $E_{HS}$/eV | $\Delta E_{HS}$/eV |
|---|---|---|---|---|---|---|---|
| TiPc-py$CH_3$ | slab | -509.63 | | | | | |
| | OH* | -520.85 | -0.35 | | | | |
| | O* | -516.74 | 0.39 | | | | |
| | OOH* | -524.93 | 3.08 | | | | |
| VPc-py$CH_3$ | slab | | | | | -510.95 | |
| | OH* | | | | | -521.82 | 0.00 |
| | O* | | | | | -517.82 | 0.63 |
| | OOH* | | | | | -526.08 | 3.24 |
| CrPc-py$CH_3$ | slab | | | | | -511.15 | |
| | OH* | | | | | -522.02 | 0.00 |
| | O* | | | | | -516.60 | 2.05 |
| | OOH* | | | | | -526.30 | 3.23 |
| MnPc-py$CH_3$ | slab | -508.51 | | -509.39 | | -509.78 | |
| | OH* | -519.12 | 1.53 | -519.65 | 1.00 | -520.07 | 0.58 |
| | O* | -514.02 | 3.26 | | | -514.74 | 2.54 |
| | OOH* | -523.39 | 4.76 | -523.94 | 4.21 | -524.32 | 3.83 |
| FePc-py$CH_3$ | slab | -508.11 | | -508.56 | | -508.76 | |
| | OH* | -518.51 | 1.13 | -518.65 | 0.99 | -518.81 | 0.83 |
| | O* | -513.48 | 2.78 | -513.47 | 2.77 | -513.18 | 3.08 |
| | OOH* | -522.94 | 4.19 | -522.92 | 4.22 | -523.02 | 4.12 |
| CoPc-py$CH_3$ | slab | -508.02 | | | | | |
| | OH* | -517.99 | 0.90 | -517.34 | 1.55 | -517.01 | 1.88 |
| | O* | -512.24 | 3.28 | -511.87 | 3.65 | | |
| | OOH* | -522.45 | 3.94 | -521.84 | 4.55 | -521.30 | 5.10 |
| NiPc-py$CH_3$ | slab | -505.30 | | | | -505.67 | |
| | OH* | | | | | -514.45 | 2.09 |
| | O* | | | | | -508.48 | 4.69 |
| | OOH* | | | | | -519.29 | 4.76 |
| CuPc-py$CH_3$ | slab | -504.40 | | | | | |
| | OH* | -512.99 | 2.28 | | | | |
| | O* | -507.04 | 4.86 | | | | |
| | OOH* | -517.97 | 4.80 | | | | |
| ZnPc-py$CH_3$ | slab | -504.16 | | | | | |
| | OH* | -512.89 | 2.15 | | | | |
| | O* | -506.55 | 5.11 | | | | |
| | OOH* | -517.45 | 5.08 | | | | |

**Supplementary Table 6.** XPS results for high-resolution N and Co for CNT and CNT-py.

| Catalyst | N content (at%) | Co content (at%) |
|---|---|---|
| CNT | - | - |
| CNT-py | 1.43 | - |
| Co HSACs | 6.15 | 0.64 |

**Supplementary Table 7.** Comparison of electrochemical $H_2O_2$ production via $2e^-$ ORR in alkaline solution.

| Catalyst | Electrolyte | Onset potential (V, @0.1 mA $cm^{-2}$) | Selectivity (%) | TOF ($s^{-1}$) | Refs. |
|---|---|---|---|---|---|
| **Co HSACs** | **0.1 M KOH** | **0.85** | **~95** | **~0.89** | **This work** |
| **CoPc** | **0.1 M KOH** | **0.78** | **~80** | **~0.12** | **This work** |
| $NiN_4$/C-$AQNH_2$ | 0.1 M KOH | 0.83 | ~80 | ~0.12 | Advanced Materials, 2104891 (2021). |
| $Co_1$-NG(O) | 0.1 M KOH | ~ 0.83 | ~ 80 | ~2.70 | Nat. Mater. 19, 436-442 (2020). |
| Fe-CNT | 0.1 M KOH | 0.822 | ~ 95 | ~0.57 | Nat. Commun. 10, 3997 (2019) |
| Co-CNT | 0.1 M KOH | ~ 0.80 | ~ 75 | ~0.34 | Nat. Commun. 10, 3997 (2019) |
| Co-POC-O | 0.1 M KOH | 0.84 | ~ 84 | ~0.21 | Adv. Mater. 31, 1808173 (2019) |
| Oxidized CNTs | 0.1 M KOH | 0.75 | ~ 89 | ~0.0178 | Nat. Catal. 1, 156-162 (2018) |
| F-mrGO | 0.1 M KOH | 0.78 | 95 | ~0.088 | Nat. Catal. 1, 282-290 (2018) |
| O-GOMC | 0.1 M KOH | ~0.82 | ~95 | ~0.10 | Chem. 7(11): 3114-3130 (2021). |

**Supplementary Table 8.** Co K-edge EXAFS spectra fitting parameters.

| Sample | Path | CN | R (Å) | $\sigma^2$ ($\times10^{-3}$ Å$^2$) | $\Delta E_0$ (eV) | R (%) |
|---|---|---|---|---|---|---|
| Co foil[a] | Co-Co | 12 | 2.50 ± 0.01 | 6.3 | 7.90 ± 0.27 | 0.05 |
| CoPc[b] | Co-$N_1$ | 4.1 | 1.91 ± 0.01 | 3.0 | 5.12 ± 1.63 | 0.6 |
| | Co-C | 8.9 | 2.94 ± 0.02 | 3.0 | | |
| | Co-$N_2$ | 4.5 | 3.26 ± 0.02 | 3.0 | | |
| Co HSACs[c] | Co-$N_1$ | 5.0 | 1.92 ± 0.01 | 2.8 | 5.35 ± 1.12 | 0.6 |
| | Co-$C_1$ | 27.3 | 2.98 ± 0.01 | 13.4 | | |
| | Co-$N_2$ | 15.5 | 3.26 ± 0.01 | 8.0 | | |
| | Co-$C_2$ | 5.9 | 3.99 ± 0.03 | 3.0 | | |
| | Co-$C_3$ | 24.5 | 4.28 ± 0.02 | 10.0 | | |

N, coordination number; R, distance between absorber and backscatter atoms; $\sigma^2$, Debye-Waller factor to account for both thermal and structural disorders; $\Delta E_0$, inner potential correction; R factor (%) indicates the goodness of the fit. $S_0^2$ was fixed to 0.76 as determined from Co foil fitting.

[a] Fitting range: $3.3 \leq k$ (/Å) $\leq 11.9$ and $1.0 \leq R$ (/Å) $\leq 2.7$.

[b] Fitting range: $2.7 \leq k$ (/Å) $\leq 11.5$ and $1.1 \leq R$ (/Å) $\leq 3.3$.

[c] Fitting range: $2.7 \leq k$ (/Å) $\leq 11.5$ and $1.0 \leq R$ (/Å) $\leq 4.0$.

**Supplementary Table 9.** Co K-edge EXAFS spectra fitting parameters of Co HSACs before and after stability.

| Sample | Path | CN | R (Å) | $\sigma^2$ ($\times10^{-3}$ Å$^2$) | $\Delta E_0$ (eV) | R (%) |
|---|---|---|---|---|---|---|
| Co HSACs before stability | Co-N | 5.0 | 1.92 ± 0.01 | 3.0 ± 1.0 | 6.81 ± 1.63 | 1.9 |
| Co HSACs after stability | Co-N | 4.9 | 1.90 ± 0.01 | 3.0 ± 1.0 | 6.03 ± 1.96 | 1.8 |

N, coordination number; R, distance between absorber and backscatter atoms; $\sigma^2$, Debye-Waller factor to account for both thermal and structural disorders; $\Delta E_0$, inner potential correction; R factor (%) indicates the goodness of the fit. $S_0^2$ was fixed to 0.82 as determined from Co foil fitting.

[a] Fitting range: $2.7 \leq k$ (/Å) $\leq 11.5$ and $1.0 \leq R$ (/Å) $\leq 4.0$.

[b] Fitting range: $2.7 \leq k$ (/Å) $\leq 12.3$ and $1.0 \leq R$ (/Å) $\leq 3.3$.

# Supplementary Note 1

**Discussion on the equilibrium potential for 2e$^-$ pathway ORR in alkaline media**

The CoPc-py-CNT HSAC exhibit the onset potential for $H_2O_2$ production at ~0.85 V vs. RHE, which is higher than the onset potential of thermodynamic limit of 0.76 V vs. RHE in alkaline solution. In acidic solution, the $pK_a$ values for the first and second ionization of $H_2O_2$ at 298 k are 11.69 ($pK_{a1}$) and ~20 ($pK_{a2}$), respectively. Therefore, the predominant hydrogen peroxide species at pH < 12 and pH > 12 are $H_2O_2$ and $HO_2^-$, respectively. In alkaline media, $HO_2^-$ is the deprotonated form of $H_2O_2$. During the LSV test, the more positive onset potential than the thermodynamic limit of 0.76 V is attributed to the Nernst related potential shift due to the relatively low concentration of $H_2O_2$ in the electrolyte[1].

$$O_2 + 2H_2O + 4e^- \rightarrow 4OH^- \qquad E_o = 1.23 \text{ V vs. RHE} \qquad (1)$$

$$O_2 + H_2O + 2e^- \rightarrow HO_2^- + OH^- \qquad E_o = 0.76 \text{ V vs. RHE} \qquad (2)$$

## References

1. H. W. Kim, M. B. Ross, N. Kornienko, L. Zhang, J. Guo, P. Yang and B. D. McCloskey, *Nat. Catal.*, 2018, **1**, 282-290.